M.Sc. Thesis

A Low-Power CMOS Wind Sensor with Corner Heaters

W.F.M. Brevet

Electronic Instrumentation Laboratory

TUDelft

A Low-Power CMOS Wind Sensor with Corner Heaters

THESIS

submitted in partial fulfillment of the
requirements for the degree of

MASTER OF SCIENCE

in

ELECTRICAL ENGINEERING

by

W.F.M. Brevet
born in Gouda, The Netherlands

This work was performed at:

Electronic Instrumentation Laboratory
Department of Microelectronics & Computer Engineering
Faculty of Electrical Engineering, Mathematics and Computer Science
Delft University of Technology

Delft University of Technology

DELFT UNIVERSITY OF TECHNOLOGY
DEPARTMENT OF
MICROELECTRONICS & COMPUTER ENGINEERING

The undersigned hereby certify that they have read and recommend to the Faculty of Electrical Engineering, Mathematics and Computer Science for acceptance a thesis entitled **"A Low-Power CMOS Wind Sensor with Corner Heaters"** by **W.F.M. Brevet** in partial fulfillment of the requirements for the degree of **Master of Science**.

Dated: 27 November 2015

Chairman: _____
prof.dr.ir. K.A.A. Makinwa

Advisor: _____
dr.ir. F. Sebastiano

Committee Member: _____
prof.dr.ir. W. Serdijn

Abstract

Compared to conventional wind sensors, such as cup and vane systems or ultrasonic anemometers, thermal wind sensors have several advantages. They are relatively low cost and very robust, as they do not require moving parts. For almost 15 years, successive generations of smart CMOS wind sensors have been developed by the E.I. Lab. In this time great improvements have been made in terms of power efficiency. Compared to the first generation sensors, which required hundreds of milliwatts of heating power, current designs only require tens of milliwatts while still achieving comparable wind sensing accuracy. These designs also feature a temperature measurement capability. However, they are still not quite ready for use in an actual product. Firstly, because of the intricate digital filter that must be applied to the output bitstreams. Secondly, improvements can be made in terms of how much electronics are required besides the sensor chip. Finally, the temperature measurements are very slow.

In this thesis, the design of a new wind sensor chip will be presented that addresses these issues. By modifying the thermal structure of the sensor the use of a very simple filter is enabled and the temperature measurement speed is increased. By integrating more electronics on-chip, its pinout has been reduced by 50%, which will reduce the manufacturing cost of a sensor system incorporating this chip. This wind sensor chip consumes 25mW of heating power and has an accuracy of $\pm6°$(direction) and ±0.6 m/s (speed), for wind speeds ranging from 4 to 25m/s.

Acknowledgments

Contents

List of Figures

List of Tables

Introduction

<div style="text-align: right">

1

</div>

Many industries, such as transportation, power generation and weather forecasting benefit from accurate and detailed information about weather conditions and, in particular, about wind conditions. Traditionally, this is obtained by mechanical sensors, which use rotating cups or propellers to measure wind speed, and moving vanes to measure wind direction. Although such sensors are often chosen because of their low cost, they suffer from mechanical wear, which limits their lifetime [1]. Moreover, when placed in a hard to reach area, for instance on a wind turbine at sea, the cost of sending a maintenance engineer to repair or replace a malfunctioning wind sensor is very high, leading to the requirement for more robust wind sensors.

There are two alternatives to mechanical wind sensors: ultrasonic and thermal wind sensors. Ultrasonic wind sensors measure wind by measuring a wind-induced change in the time of flight of an acoustic signal[2] or the change in phase of an acoustic resonating signal[3]. They require only several milliwatts of power and do not have moving parts. However, they are quite expensive, with prices starting above \$1000.

Thermal wind sensors determine wind speed and direction by measuring the change in the temperature distribution of a heated sensing element that is cooled by the wind. From this information, both wind speed and direction can be calculated. This sensing method also does not require moving parts. To improve their usability and robustness, thermal wind sensors can be made "smart"'. This means that they should combine the sensor and the read-out electronics in the same package and provide a robust digital output signal. This minimizes the need for additional external electronics, and reduces the cost and size of the resulting sensor system.

Thermal wind sensing with CMOS-compatible devices has been the object of research at the Delft University of Technology since the late eighties[4]. The aim is to combine the high-volume manufacturing and precision electronics of a CMOS process with a sensor on a single chip. In the first designs, the sensor chip only contained the sensing part of the system, i.e. the heated sensing element[4, 5]. The read-out electronics was placed on a separate PCB. The biggest drawback of this system is that it requires a significant trimming operation for every sensor, due to spread in the thermal behavior due to packaging tolerances. The read-out circuitry was integrated on-chip in the next design[6]. The read-out was implemented as a thermal balancing, or thermal sigma-delta (T$\Sigma\Delta$), loop. With this the need for a manual trim greatly decreased and the amount of discrete circuitry was reduced. The system now supplied a digital bitstream directly to an external microcontroller. This design required 450mW of heater power. To reduce the amount of heater power and improve the sensor's performance an electrical integrator was added to the loop[7, 8]. This greatly improved the sensor's resolution and reduced the required heater power to 25mW. Also, it made the on-chip thermal balancing loop oscillate at a frequency dependent on the thermal delay

of silicon, adding temperature measurement capability to the sensor. The conversion time for this temperature measurement was 8 seconds. These wind sensors[6, 7, 8] have demonstrated that low inaccuracy ($\pm 4\%$ for speed and $\pm 2°$ for direction) and low power are possible with a single chip design in conventional CMOS technology without using MEMS techniques.

The main focus of prior work has been the optimization of the interface electronics [6, 7, 8], while retaining the same basic thermal design as in [4]. This work describes a wind sensor with an optimized layout and a new thermal design. This resulted in improved thermal dynamics, simpler decimation and better area efficiency, while maintaining similar wind sensing performance. The temperature measurement was expected to improve with this change, but in the end this was not found to be the case. The number of connections between the sensor chip and the outside world was reduced, by the addition of on-chip control and clock derivation logic, thus reducing manufacturing costs and simplifying the entire sensor system. Furthermore, several different heater driving schemes were implemented to test whether the operation of the sensor can be improved by lowering the differential heater power, while keeping the total heater power equal.

This work is organized as follows. In chapter 2 the operation of the sensor's wind and temperature measurements, the specifications of the previous design and what will be improved upon is discussed. Chapter 3 will first describe the system-level design and afterwards the circuit-level design of the new sensor chip. The measurements of the new chip are presented in chapter 4. Chapter 5 contains the conclusions drawn from the work presented in this thesis.

Operating principles

2

The smart wind sensor presented in this thesis measures wind by digitizing the thermal imbalance caused by wind flowing over the sensor surface. In this chapter the operating principles of the sensor are explained. First the general principle of thermal wind sensing is introduced. Afterwards the readout principle implemented on chip, called thermal sigma-delta modulation, or thermal balancing, is explained. The sensor's calibration model and the use of the wind sensor as a temperature sensor are explained. The chapter concludes with a section detailing the specifications of the previous chip and what will be improved upon.

2.1 Thermal Wind Sensing

Thermal wind sensing involves the determination of wind velocity via its effect on the thermal state of a sensor. To be able to do this, power needs to be dissipated in the sensor to increase its temperature (slightly) above ambient temperature. Wind flowing over the sensor will asymmetrically cool it, i.e. the upstream part of the sensor will be cooled more than its downstream part. This creates a thermal imbalance as shown in figure 2.1. This figure shows a cross-section of the sensor chip, which is glued to a ceramic disk protecting it from the environment. The wind will flow over the top of the ceramic disk, ensuring that the chip is protected from the environment but still in good thermal contact with the air flow. The color gradient shows the thermal imbalance that is caused by wind flowing over the ceramic disk; the blue area is at ambient temperature and the red area is at a slightly higher temperature.

The cooling of the sensor due to the wind can be described with equation 2.1, the generalized version of King's law:

$$\frac{P}{\Delta T} = A + BU^n \tag{2.1}$$
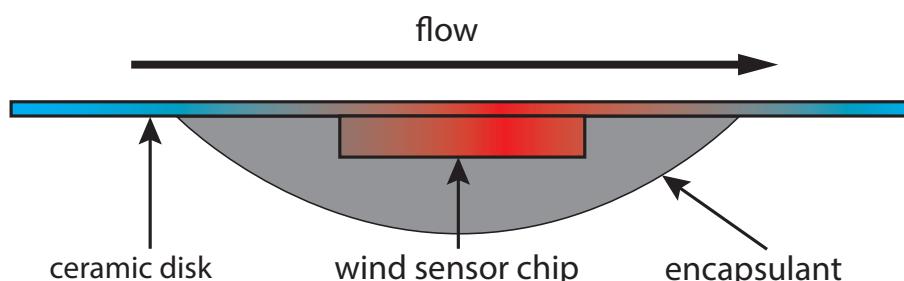
Figure 2.1: This figure shows a cross-section of the sensor system.
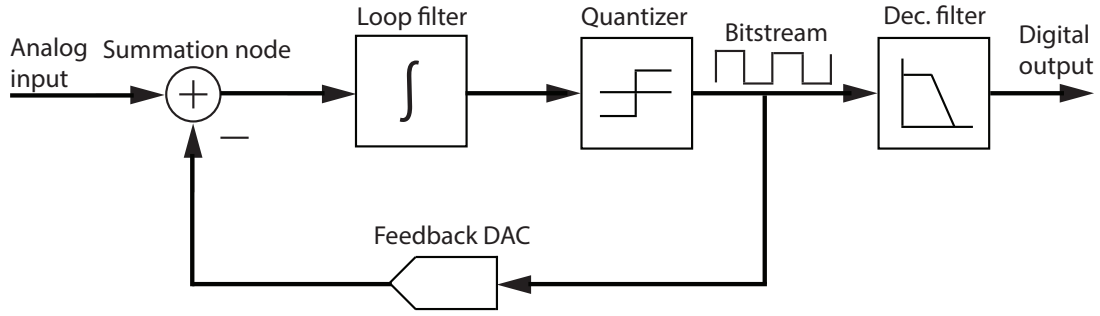
Figure 2.2: This figure shows the a block diagram of a basic sigma-delta modulator and its decimation filter.

Where P is the heating power dissipated in the sensor; U is the flow speed; A and B are constants; ΔT is the overheat, the difference between the temperature of the exposed surface and the ambient temperature; n is a constant that is dependent on whether the flow is laminar (n is 0.5) or turbulent (n is 0.8). The flow speed can be calculated when both P and ΔT are known. The direction can be calculated if several flow sensors are arranged in such a way that they measure different components of the flow velocity. From this equation, two ways of operating a thermal sensor are found. ΔT can be kept constant, while measuring P or vice versa. Keeping ΔT constant requires an extra temperature sensor for the system, while keeping P constant does not. Since a simple system is the goal of this design, keeping P constant is better suited. The sensor will thus be operated in the so-called constant power mode.

The smart wind sensor has developed from an open loop sensing system[4, 5] to a closed-loop, thermal balancing system[9, 10]. The adaption of a closed-loop systems has several benefits. It increases the linearity of the system and relaxes the requirements of the interface electronics. The loop is closed by letting the output of the interface electronics control the on-chip heaters. This creates a thermal balancing, or Sigma-Delta, loop that will digitize thermal imbalances on the chip. In prior art[8], it was found that the addition of an electrical integrator to the loop increases resolution and enables temperature measurement with the wind sensor. In the following sections the operation of this closed-loop system will be explained.

2.2 Thermal Sigma-Delta modulation

The sensor uses thermal Sigma-Delta ($\Sigma\Delta$) modulation to digitize the thermal imbalance that is created by wind flowing over the sensor. First $\Sigma\Delta$ modulation will be introduced and afterwards it will be shown how this concept is implemented in the sensor chip.

2.2.1 Sigma-delta modulation

$\Sigma\Delta$ modulation is a method of performing Analog-to-Digital Conversion (ADC). The value or signal to be digitized is first encoded into a high-frequency, low-resolution bitstream. This bitstream is then filtered with a digital decimation filter in order to

obtain a digital representation with the required resolution and frequency. Sigma-Delta modulators are widely used in electronics because they leverage the high frequencies at which modern IC processes can operate to obtain accurate ADCs and DACs with relaxed requirements of their analog circuit parts.

Figure 2.2 shows the basic structure of a $\Sigma\Delta$ Modulator and its decimation filter. The $\Sigma\Delta$ modulator converts the analog input signal to a bitstream. The quantizer provides a digital approximation of the loop filter output signal by sampling it at frequency Fs. The digital approximation can be quite crude, which causes a quantization error. The quantization error can be modeled as white noise between DC and $F_s/2$. To reduce the quantization noise, the comparator is run at a higher frequency then dictated by the Nyquist criterion; the $\Sigma\Delta$ modulator is thus an 'oversampled' ADC. Due to the oversampling, the quantization noise is spread out over a wider bandwidth than the signal bandwidth. This lowers the amount of noise in the signal bandwidth. The use of feedback with a loop filter can shape the spectral power of the quantization noise to frequencies outside the band of interest; this is called noise shaping. The digital output of the quantizer is converted back into an analog signal by the feedback DAC and then subtracted from the input signal at the summation node to close the feedback loop. By combining the noise shaping effect with oversampling, a high resolution ADC can be made with a low-resolution quantizer.

The bitstream output of the $\Sigma\Delta$ modulator is filtered by a decimation filter to construct the high resolution, digital representation of the input signal by filtering out quantization noise outside the signal bandwidth. The decimation filter consists of a digital low-pass filter and a downsampling action. The low-pass filter removes the high frequency noise content shaped by the loop filter. Downsampling reduces the sample rate to the required rate. The complexity of the low-pass filter depends on the amount of filtering needed to remove all the noise. The simplest filter is a normal averaging filter, i.e. a sinc filter. Since it is a FIR filter with equal weights for all its coefficients, it is easy to implement and cheap, but it provides limited filtering. More aggressive filters can be constructed by choosing other weights for the coefficients, but it is evident that this will make the filter's implementation more difficult.

2.2.2 Loop architecture

The smart wind sensor chip has two $\Sigma\Delta$ modulators that digitize the thermal imbalance on the sensor. One modulator works along the North-South axis of the chip; the other works along the East-West axis. This enables the measurement of wind speed and direction for wind coming from any angle in the plane of the sensor. The $\Sigma\Delta$ loops on the chip are so-called hybrid, (pseudo) 2nd order loops. They are called hybrid because a part of the loop is in the thermal domain and a part is in the electrical domain and 2nd order because there are (at least) two poles present in the loop filter.

The thermal part of the sensor is formed by an Electro-Thermal Filter (ETF). It consists of the heaters, the thermal mass of the substrate and the sensing part, i.e. the thermopiles. This filter has the thermal state of the sensor as its input and its output is a voltage proportional to any thermal imbalance. The ETF can be modelled as a
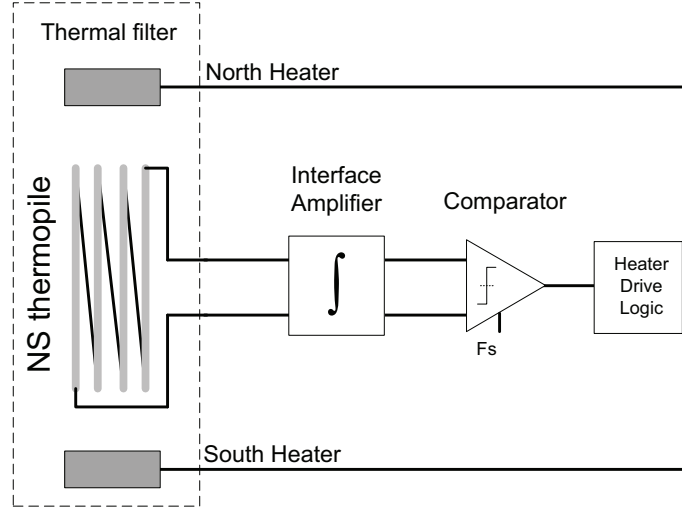
Figure 2.3: This figure shows the structure of the hybrid sigma-delta modulator loop on the wind sensor chip.
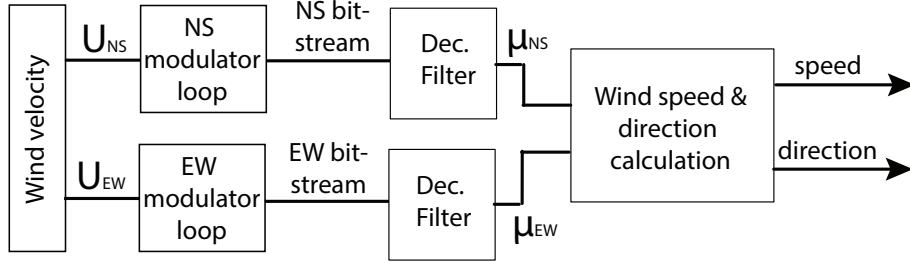
Figure 2.4: This figure shows a block diagram of the wind sensor.

ladder network of thermal resistances and capacitors and thus exhibits a multi-pole low-pass filtering behavior.

Figure 2.3 shows the architecture of one of the two loops. The ETF is followed by an electrical integrator, a comparator and some logic. In the structure of the loop on the wind sensor chip, the basic sigma-delta modulator loop structure shown in 2.2 can be found. The feedback DAC is implemented by the heaters. The summation takes place in the thermal mass of the substrate. This mass, the thermopiles and the integrator together form the loop filter and the clocked comparator is a 1-bit quantizer. The decimation filter is applied to the bitstream off-chip.

2.3   Wind sensor model

Figure 2.4 shows a block diagram of the entire sensor system. The wind velocity is split into its North-South (NS) and East-West (EW) components. The sensor chip contains a modulator loop for each component. The output bitstreams are fed into the off-chip decimation filter to produce the digital values μ_{NS} and μ_{EW}. The model that is used to calculate wind speed and direction from these values is discussed in this section.

For wind speed, a 2-dimensional, 5th order polynomial is fitted on μ_{NS} and μ_{EW} versus wind speed. This data is obtained from a calibration measurement in a wind tunnel. The wind speed is calculated by evaluating this polynomial for a measured set of μ_{NS} and μ_{EW}.

To calculate the direction a physics based calibration model is used; this model is given by equations 2.2 and 2.3 [11]:

$$\mu_{NS} = (\frac{\sqrt{U}}{A_{NS} + \sqrt{U} \cdot B_{NS}}) \sin(\theta + \delta_{NS}) + \sqrt{U} \cdot D_{NS} + E_{NS} \qquad (2.2)$$

$$\mu_{EW} = (\frac{\sqrt{U}}{A_{EW} + \sqrt{U} \cdot B_{EW}}) \cos(\theta + \delta_{EW}) + \sqrt{U} \cdot D_{EW} + E_{EW} \qquad (2.3)$$

In the equations, μ is the decimated output of each respective loop. $\sqrt{U}$ is the square root of the wind speed in m/s. A and B are gain calibration parameters. θ is the angle of the wind. δ is the angle offset of the sensor. D and E are wind dependent and static offset terms, respectively. For each modulator loop, a set of the parameters A, B, δ, D and E is determined by calibration of the sensor in a wind tunnel. The model equations can then be evaluated to obtain θ, the angle of the measured wind. To calculate the angle for a set of measured $\mu_{NS,EW}$, equations 2.2 and 2.3 are solved for the values of the sine and cosine. The arctangent of the fraction between the sine and the cosine is calculated and correct for the offsets $\delta_{NS,EW}$ to produce the angle:

$$\theta = \arctan \frac{\sin(\theta + \delta_{NS})}{\cos(\theta + \delta_{EW})} - \frac{\delta_{NS} + \delta_{EW}}{2} \qquad (2.4)$$

Specifications for the quantization resolution and the linearity of the modulator loop can be derived from this model. Assuming the same signal amplitude will be achieved in the measurements as in the previous work, the angle error due to these nonidealities was calculated and plotted in figure 2.5. From this graph is seen that to calculate the angle with 1° accuracy, the modulator's accuracy must be greater than 7.9 bits.

2.4 Temperature sensing

In [10], it was shown that the wind sensor can also be used to measure temperature. To do this, the frequency of oscillation of the output bitstream is observed. This oscillation is caused by having an integrator and an ETF in a feedback loop, as is shown in figure 2.6. Together the filters produce 180° of phase delay, which causes the oscillation. The electrical integrator has a stable phase delay of 90° over a wide frequency range. The phase delay of an ETF is found to be[12]:

$$\phi_{ETF} \propto s\sqrt{fT^{1.8}} \qquad (2.5)$$

From 2.5 it can be seen that the phase delay is proportional to the distance between heater and sensor, s, and also depends on the frequency of the signal, f, and the temperature, T. When the system is oscillating, the phase delay of the ETF is exactly

Angle error due to nonidealities
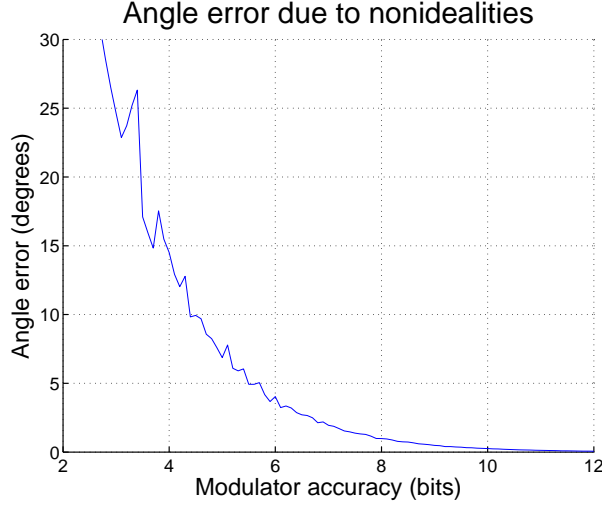
Figure 2.5: This graph shows the angle error due to nonidealities of the modulators.

ETF   E. Integrator   Comparator

$\varphi \propto \sqrt{(f\,T^{1.8})}$ $\varphi = 90^0$ Fs
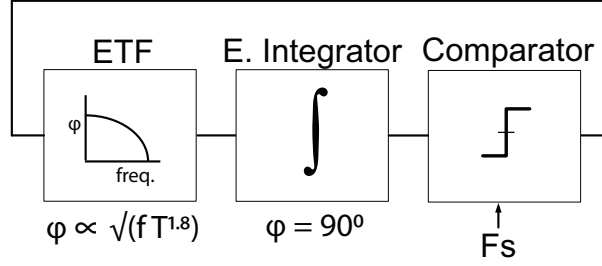
Figure 2.6: This figure shows a simplified diagram of the modulator loop with its ETF and integrator.

90 degrees and so a direct relation between oscillation frequency and temperature is found:

$$\frac{1}{f} \propto T^{1.8} \tag{2.6}$$

In the prior art[10], the oscillation frequency is around 30Hz. To get an accurate estimation of this frequency, a relatively long measurement is required. The temperature measurements of the previous chip take 8 seconds per conversion.

2.5   Prior work

The specifications of the chip presented in [10] are summarized in table 2.1. The design of that chip is used as a basis for the work that is presented in this thesis.

The design presented in this thesis will be focused on improving the chip in two ways: improving the temperature measurement and simplifying the entire system. The

Parameter	Value
Total heater power	25mW
Sampling frequency	15kHz
Oscillation frequency	30Hz
Accuracy (wind speed)	$\pm 4\%$
Accuracy (wind direction)	$\pm 2°$
Conversion time (wind)	1s
Accuracy (temp.)	$\pm 1°C$
Conversion time (temp.)	8s
Resolution (temp.)	$\pm 0.15°C$
No. of bond wires	16

Table 2.1: This table summarizes the specifications of the previous wind sensor chip.

first goal is to decrease the conversion time for the temperature measurement from 8s down to 1s.

Second, the system will be simplified by implementing most of the control logic on-chip. This will reduce the off-chip component count of the system, therefore reducing the manufacturing costs. An added benefit is that the number of bond wires required for the chip is minimized, thus further reducing manufacturing costs.

The accuracy of the sensor must not suffer from those changes. The sensor already provides wind measurements with comparable accuracy to conventional wind sensors and the temperature measurement is sufficiently accurate for meteorological applications, i.e. it does not require any improvement.

Design

3

In this chapter the design of the wind sensor chip will be discussed. The main aim of this design is to improve the usability of the wind sensor so that it can be easily turned into a product. This will be achieved by adopting a simpler decimation scheme and by integrating more functionality on-chip so as to minimize the amount of external control signals required. By integrating most of the control logic on-chip, the amount of off-chip electronics is minimized, thus reducing the production costs. Moreover, reducing the amount of control signals leads to fewer bondwires. First, this will decrease manufacturing costs. Second, it will decrease the amount of heat that leaks away through the bondwires and therefore increase the thermal efficiency of the design.

In previous work, a tracking $sinc^2$ filter has been used as decimation filter. This required multiplication on an input bitstream by triangular-weighted coefficients, and adaptive tuning of the filter length to the period of the sensor's main limit-cycle[10]. As this would be computationally intensive for a low-cost microcontroller, in the proposed design the oscillation frequency is shifted to a higher frequency so that the decimation filter can be simplified.

This chapter is organized as follows. First the system-level design will be discussed. The speed-up of the thermal filter, the different operating modes, the heater layout and the error budgeting of the temperature measurement will be discussed. In the following section, the circuit-level design is presented; different parts of the design will be discussed, starting with the thermopiles, followed by the heaters, the electrical integrator, the comparator and the control logic. The chapter closes with some layout considerations for the wind sensor required to minimize parasitic coupling effects and thermal imbalance.

3.1 System-level design

In this section the system level design of the wind sensor is presented. First, the speed-up of the thermal filter is explained. Then, the two new operation modes of the wind sensor, i.e. One-Heater and Return-to-Heat mode, are introduced. Afterwards, the layout of the corner heaters is explained. This section closes with a discussion of the error budget for the components of the chip.

3.1.1 Speeding up the thermal filter

To use a simpler decimation filter in the wind sensor, the frequency of the sensor's oscillation must be increased so that the filter provides enough attenuation to the quantization noise. The simplest decimation filter possible is the fixed-length $sinc^1$
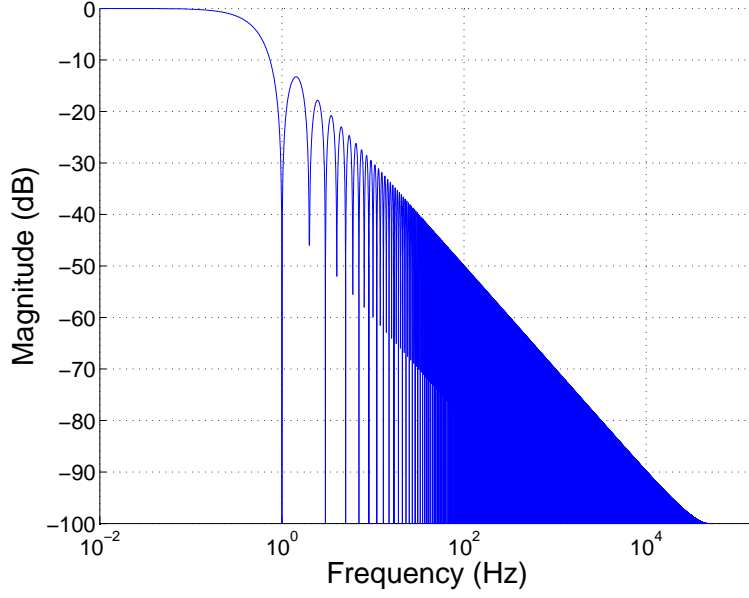
Figure 3.1: This figure shows the frequency response of a $sinc^1$ filter.

filter. This filter has equal weights for all its inputs. Filtering the bitstream with this filter is equal to a normal averaging function. In figure 3.1 the frequency response of a $sinc^1$ filter is shown. The spectrum of the output bitstream observed in the prior work is shown in figure 3.2. For 2nd order $\Sigma\Delta$ operation, the quantization noise is located at the oscillation frequency around 30Hz and its harmonics. To ensure that the $sinc^1$ filter properly attenuates the quantization noise, the oscillation frequency must be increased to the point where the filter provides an attenuation of 70dB. For a $sinc^1$ filter with a length of 1 second, clocked at 150kHz, this attenuation is achieved at frequencies larger than 1kHz. Since the oscillation frequency is about 30Hz in the prior art, this has to be increased by a factor of 33 to enable the use of a $sinc^1$ decimation filter.

The oscillation will appear at the frequency at which the total loop's phase delay is 180°. Since the electrical integrator has a constant phase shift of 90°in the relevant frequency range, the oscillation frequency will be equal to the frequency at which the phase delay of the thermal filter is exactly 90°. For a thermal filter, the pahse delay, ϕ_{ETF}, depends on the distance between the heater and the thermopile, s, the temperature, T, and the frequency of the signal, f, and is found to be 3.1 [12]:

$$\phi_{ETF} \propto s\sqrt{fT^{1.8}} \tag{3.1}$$

To increase the frequency at which the phase shift is 90°by a factor of 33, the distance between the heaters and the thermopile has to decrease by at least a factor of $\sqrt{(33)} \approx 5.7$. In figure 3.3 the location of the heaters of the previous designs[8, 6] and the new design are shown. The distance between the heaters and the thermopiles in the previous chips, marked as D_{old}, is about 1mm. In the new design this distance is reduced by placing the heaters in the corner of the chip. The new distance is marked as D_{new} and measures about 0.15mm. This modification is expected to increase the oscillation
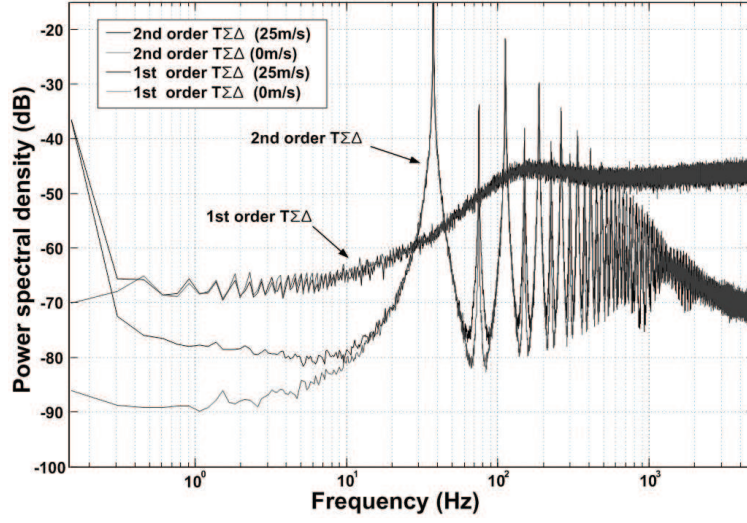
Figure 3.2: This figure shows the spectrum of the output bitstream of the previous work.
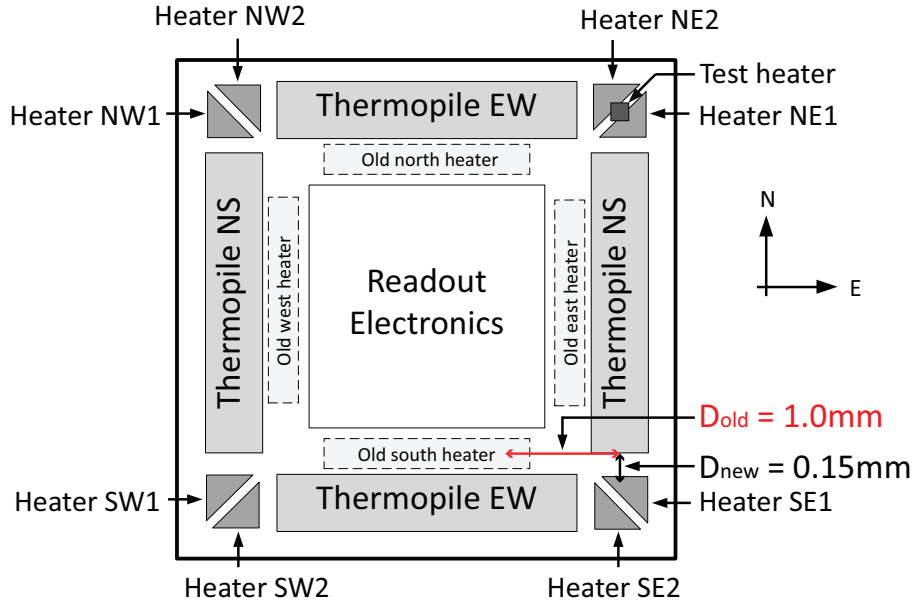
Figure 3.3: This figure shows the new and the old heater placement on the sensor chip with marked distances.

frequency by a factor $(1/0.15)^2 \approx 44$ to around 1300Hz, which is well above the required 1000Hz.

3.1.2 Operation modes

Two new operation modes for the sensor are introduced in this design; the One-Heater(1-H) mode, which is an experimental mode enabled by the adoption of corner heaters and the Return-to-Heat mode, which will optimize the dynamic range of the
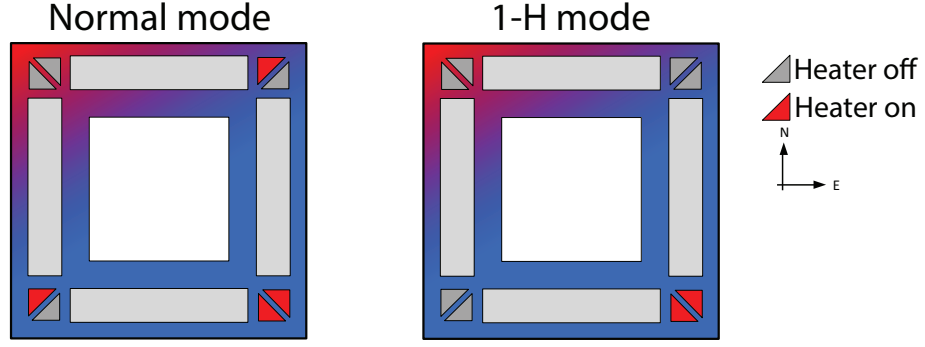
Figure 3.4: This figure shows the difference between the reaction of the chip to thermal imbalance in normal and One-Heater modes.

modulators.

There are two ways of activating the heaters to resolve a thermal imbalance. The sensor could activate both heater halves associated with one of the loops at a certain side of the chip. For example, a positive thermal imbalance on the North-South axis of the system, i.e. the north side of the chip is warmer, is corrected by activating heaters SW1 and SE1. A negative thermal imbalance on this axis is corrected by activating heaters NW1 and NE1. This works similarly on the East-West axis, but with the heaters NW2 and SW2 or NE2 and SE2 for positive or negative imbalances. This will resemble the operation of the previous design and is thus called normal mode.

When operated in 1-H mode, the data from both axis is combined and the imbalance is resolved by turning on the heaters in one corner only. For example, when a positive thermal imbalance exists on the North-West of the chip, the system will react by turning on heaters SE1 and SE2 in the South-East corner. Because of the sensor's large thermal inertia, it should still operate.

Figure 3.4 illustrates the difference between the normal and 1-H modes. The figure shows two simplified drawings of the sensor chip with a thermal imbalance. The North-West corner is hotter than the rest of the chip; the resulting thermal gradient is illustrated by the color gradient in the substrate. The heaters are drawn in two different colors; grey for when they are turned off and red when they are turned on. In the left drawing the sensor is operating in normal mode and in the right drawing it is operating in 1-H mode.

The wind sensor designed in [8] uses only a small portion of the dynamic range of the thermal Sigma-Delta Modulator. For wind speeds ranging from 0 to 25m/s, the output of each modulator is within [-0.2, 0.2], while the total available range is [-1,1]. Since the quantization noise is proportional to the total available range, this may limit the SNR.

To improve the range used by the system, the references of the modulator can be scaled down, thus reducing the quantization noise. This is done by lowering the differential power dissipated by the heaters. However, since the total dissipated power must remain the same to maintain proper sensor performance, common-mode heat must
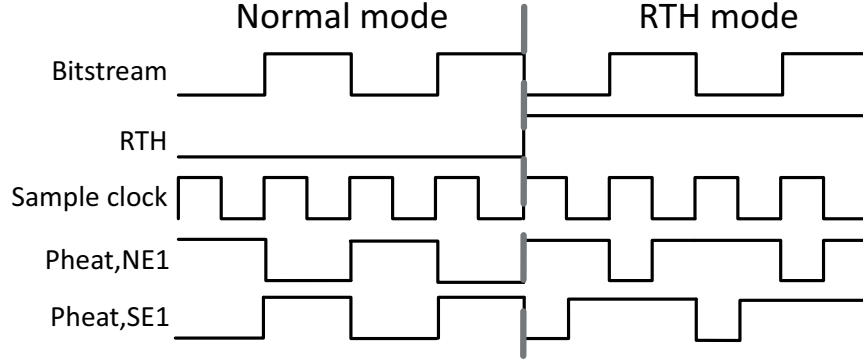
Figure 3.5: This figure shows the difference between the driving of the heaters of the NS modulator in normal and RTH modes.

be dissipated. The 'Return-to-Heat' (RTH) mode was developed to accommodate this. The wind sensor now has two modes of operation, the normal mode and RTH mode. When operated in normal mode, the heater selected in each cycle is turned on for the full duration of the sampling clock cycle. When RTH is activated the sampling clock cycle is divided into two halves. During the first half, only the heaters selected to cancel the thermal imbalance are turned on. During the second half, all the heaters will be turned on to add common-mode heat. Figure 3.5 shows the difference in the heater driving signals between these two modes. In the first half of the displayed waveform the sensor is operated in normal mode and in the second half it is operated in RTH mode. $P_{heat,NE1}$ and $P_{heat,SE1}$ denote the heater driving signals of the heaters NE1 and SE1. These are heaters for the NS modulator on the eastern side of the chip on respectively the north and the south side of the thermopile.

3.1.3 Corner heater layout

Comparing the heater layout of the previous designs to that of the new design, the heater on one side of the chip is split into two parts, one in each corner adjacent to that side. For example, the 'Old North heater' is split up into the heaters NE1 and NW1, as shown in figure 3.3. Any mismatch between these two parts may cause a thermal imbalance and thus cross-talk between the NS and the EW T$\Delta\Sigma$ modulators. This has been minimized by maximizing their area and by realizing them as diffusion resistors, since these match better (in this process) than the polysilicon resistors used in prior work. To make the heaters as large as possible, the double-L shape shown figure 3.6 is used. The North-West (NW) heater is shown, but the other heaters have exactly the same layout rotated to keep the orientation with respect to the neighboring thermopiles equal for all corners. Each corner contains two 'heater halves': the red and blue diffusion resistors, which are driven by the heater driving signal from their respective modulators. For the NW corner, heater driver A and the red heater are controlled by the EW modulator (NW2 in figure 3.3) and heater driver B and the blue heater are controlled by the NS modulator (NW1 in figure 3.3) . The black square contains two large heater driving transistors. The yellow test heater is a polysilicon
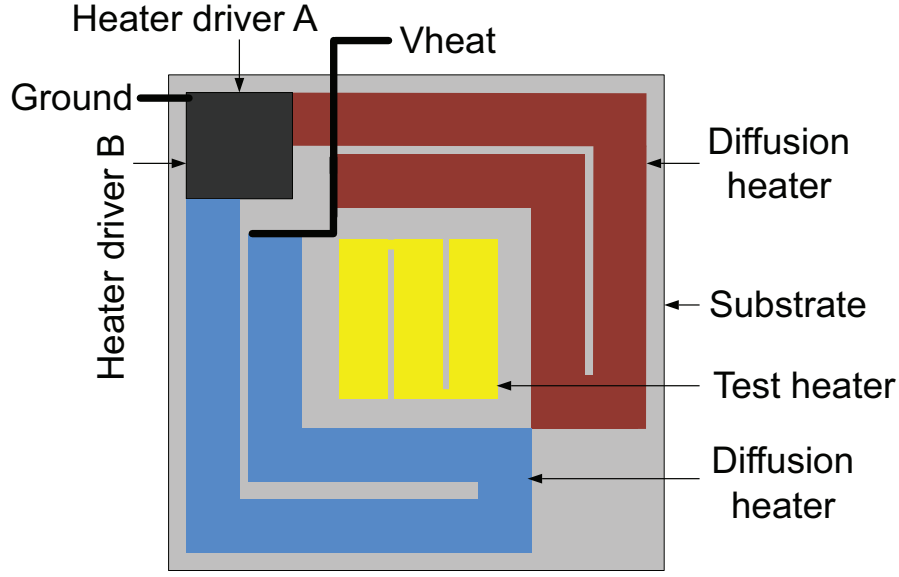
Figure 3.6: This figure shows the layout of the North-West heater.

resistor and is only connected in the North-Eastern corner of the chip. This layout has several advantages. First, it allows the heaters for both the NS and the EW T$\Delta\Sigma$ modulators to be placed in the corner, while leaving enough space between them for a test heater used for characterization. Second, the heaters are as large as possible to minimize mismatch. Third, the heater layout is highly symmetrical around the sensors diagonal, thus minimizing the crosstalk between the modulators.

The N+ diffusion resistor in this process has a square resistance of $67.5\Omega/\square$. To maximize the matching between the four corners' heaters, the resistors are made so they fill the entire space in their corner. The resulting resistors have in a width of 80μm and are 11.5 squares large. The resistance per heater half is 776Ω. The maximum total heater power is 120mW at a heater supply voltage of 5V. This voltage is supplied through an external pin, to be able to vary the amount of power dissipated in the heaters and determine its optimum value through experiments.

3.1.4   Requirements for the temperature measurement

To ensure an accurate temperature measurement, the phase delay that is introduced by the components is budgeted before the actual design. The aim of this design is to produce a system that can measure temperature accurately with a simple calibration. The error caused by a constant phase delay is calibrated out during batch calibration, but the error caused by spread of the phase delay within the batch is not. In this section the maximum tolerable phase delay for the required temperature accuracy is derived. This will be used during the design as a vital specification for parts of the chip.

The phase delay of the ETF is given by equation 3.1. The sensitivity function of
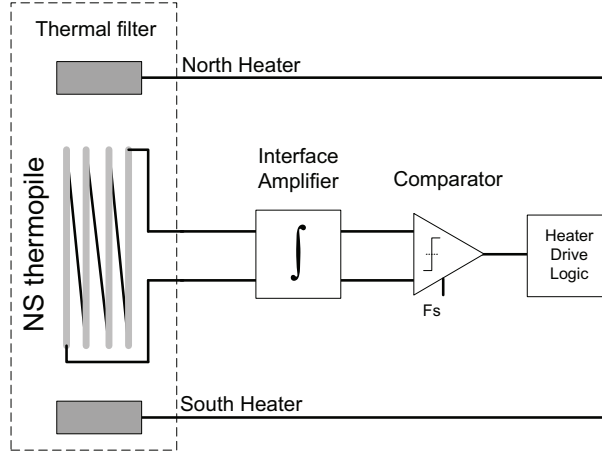
Figure 3.7: This figure shows a block diagram of the sensor system.

the systems temperature measurement to phase can be calculated from this equation:

$$S_{phase} = \frac{\delta T}{\delta \phi_{etf}} \tag{3.2}$$

The maximum value of this function was calculated to be $3.7°C/°$. For the specified accuracy of $0.1°C$, this translates into a maximum phase spread budget of:

$$\phi_{error} = \frac{\pm Accuracy}{\max(S_{phase})} = \pm 0.135° \tag{3.3}$$

$$\phi_{budget} = 2\phi_{error} = 0.27° \tag{3.4}$$

This phase budget has to be shared between the spread of the phase delay of the thermopiles and that of the electrical integrator.

3.2 Circuit-level design

With the new placement of the heaters the characteristics of the sensor will change. The other circuit parts have to be redesigned to cope with these changes and to assure that the error budgeting is met. Figure 3.7 shows a simple block diagram of one of the two balancing loops of the wind sensor. In the following sections the design of the different circuit parts shown in this figure is presented.

3.2.1 Thermopiles

The thermopiles are the sensing element of the wind sensor chip. A thermopile is formed by the series connection of a number of thermocouples, or 'arms'. The thermocouples are made by creating two strips of different conductive materials on top of each other on the chip and connecting these at one side. Their operation is based on the Seebeck effect, that is the direct conversion of a temperature difference to an electrical voltage.

17
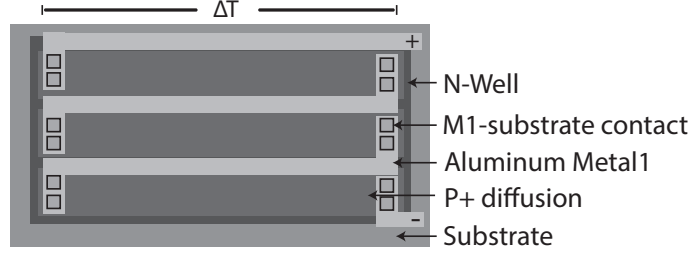
Figure 3.8: This figure shows the layout of the thermopiles in the substrate.

Thermopiles are the ideal choice for the sensing part, because they are inherently offset-free[9]. This property is beneficial for the wind sensor because the thermal balancing loops only sense which of the sides of the chip is hotter than the other and balance this accordingly.

The thermocouples are made by the series connection of P+ diffusion resistors and aluminum interconnects. Figure 3.8 shows the layout of the thermopiles in the substrate. A temperature difference between the left and right side, ΔT, will result in a voltage difference between the + and - terminals of the thermopile.

The thermopiles can be seen as a series connection of voltage sources with a lumped RC model for their resistance and their parasitic capacitance. The parasitic capacitance is the junction capacitance between the P+-thermocouples and the N-well, in which they are made. This capacitance is affected by the voltage over the junction. To minimize the phase delay of the thermopiles, this capacitance must be as small as possible. The junction capacitance is smallest when the voltage across the PN-junction is as negative as is possible. Therefore, the N-well is biased at 5V and the thermopiles at 0V.

The area used by the thermopiles determines the Signal-to-Noise Ratio (SNR) of the sensor [12]. To compare the performance of the proposed sensor fairly to the previous work, this area is kept the same. As the total area is fixed through this constraint and the length of each thermopile is fixed by the chip's dimensions, the total width per thermopile is also fixed. However, the amount of thermocouples per thermopile can be varied. There is a direct relation between the number of thermocouples per thermopile and the width of each thermocouple:

$$W_{total} = N \cdot W_{thermocouple}$$

Where $W_{total,thermocouple}$ is respectively the total width of a thermopile or the width of one thermocouple and N is the number of thermocouples in a thermopile. Increasing the number of thermocouples per thermopile will increase the signal coming from the thermopiles; each additional thermocouple adds an additional Seebeck voltage to the total thermopile output. Even though the SNR is fixed by the thermopile area, a larger signal will reduce the effect of noise present in the circuit. This comes at the cost of decreased thermocouple width and therefore an increase in resistance. Based on the geometry, expected values for the resistance and the parasitic capacitance of the thermopile arms can be calculated. The previous design has thermopiles with 12
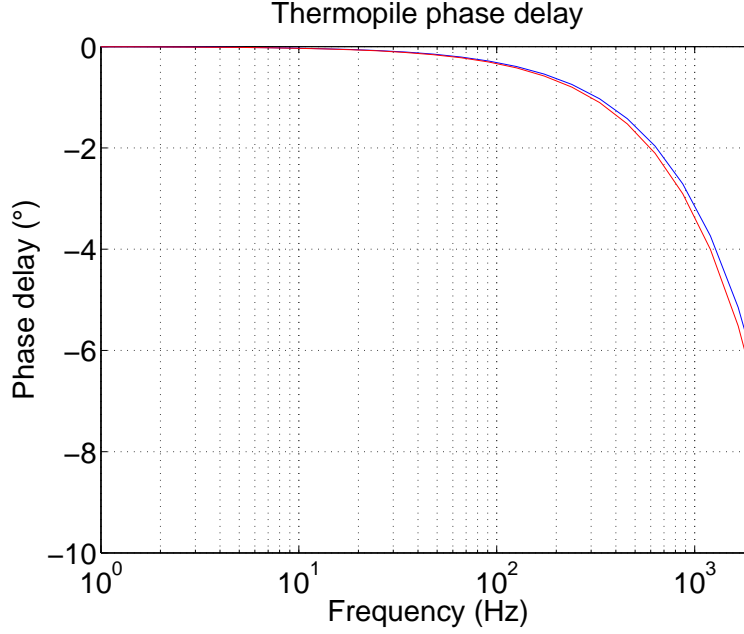
Figure 3.9: This figure shows the phase delay of the thermopile versus frequency in high and low process corners.

arms. For these, the total nominal resistance per thermopile is 168kΩ. The junction capacitance is calculated to be around 41pF per arm.

To quantify the effect of the phase delay spread, a simulation was done in which the process spread of the thermopile's resistance and capacitance was observed. The design manual for this particular CMOS process, [13], specifies that the resistance of the P+ resistors used in the thermopiles can spread by ±15% and that their parasitic capacitance can spread by ±22%. The effects of a constant phase delay will be calibrated out by batch calibration, so only the inter-batch spread will influence the accuracy of the measurement. This was assumed to be 10x smaller than the entire spread. Figure 3.9 shows the thermopile's phase delay for different process corners. At the expected oscillation frequency, 1300Hz, the difference between the high and low cases is around 0.29°. The spread of the thermopile already consumes the entire phase spread budget which was derived in section 3.1.4. Increasing the number of thermopile arms will increase the phase delay and also its spread, which will rapidly reduce the accuracy of the sensor. The number of arms was kept at 12 for this reason.

The thermal noise voltage density of the thermopile is calculated with equation 3.5:

$$V_{n,tp} = \sqrt{4kTR_{tp}} \tag{3.5}$$

Where k is the Bolzmann constant, T is the temperature in Kelvin and R_{tp} is the thermopile's resistance. The thermal noise voltage density at 20°C is calculated to be $52nV/\sqrt{Hz}$.

19

3.2.2 Electrical Integrator

In previous work[10], it is shown that the addition of an electrical integrator in the thermal balancing loop improves the performance of the wind sensor. With its addition, two integrators are present in the loop: the lossy thermal integrator and the high-DC-gain electrical integrator. Because of the two integrators in the loop, the sigma-delta modulator will exhibit second-order behavior, which means that it will have increased quantization noise rejection. The derivation of the specifications for the integrators g_m remains mostly the same as [10].

Either voltage or current read-out can be used to obtain a good readout of the thermopile's signal. In this design voltage read-out is used and so the integrator must have a much higher input impedance then the thermopile's impedance.

The thermopiles are the main sensing elements of the system and so, their noise should be the dominant thermal noise source. This means that the noise contribution of the integrator must be smaller. The thermal noise density of the thermopile is calculated from equation 3.5 and is $52nV/\sqrt{Hz}$.

The input common-mode voltage of the integrator is set by the bias voltage of the thermopiles. The parasitic junction capacitance between the P+-thermocouples and the N-well in which they are situated is minimized when the junction voltage is as low as possible. Therefore, the input common-mode voltage is set to 0V.

Chopping is used to decrease the offset of the integrators amplifier and remove any $1/f$-noise. The $1/f$-noise corner of a CMOS device in the used $0.7\mu m$ process lies at around 1kHz for typically sized input devices. The chopping frequency must be higher than this to completely remove the noise. System-level chopping is used to reduce the residual offset even further. To gain as much as possible from the system-level chopping, it must be operated at the lowest possible frequency. The system will operate with a conversion time of 1 second, so the system-level chopping frequency is set to 1Hz.

At the oscillation frequency the integrator must have an accurate $90°$ phase delay to make an accurate temperature measurement. The accuracy of this phase delay depends on the distance between the integrators pole frequency and the oscillation frequency.

The transfer function of the integrator is:

$$\frac{V_{out}}{V_{in}} = \frac{-1}{1 + j\frac{\omega}{\omega_p}} \tag{3.6}$$

from which the phase delay of the integrator is derived to be:

$$\angle\frac{V_{out}}{V_{in}} = \arctan\frac{\omega}{\omega_p} \tag{3.7}$$

where ω is the angular frequency and ω_p is the pole frequency. Assuming a spread of 10% in the pole frequency location, the phase delay spread of the integrator is given by 3.8:

$$\phi_1 - \phi_2 = \arctan\frac{\omega_{osc}}{1.05\omega_p} - \arctan\frac{\omega_{osc}}{0.95\omega_p} \tag{3.8}$$
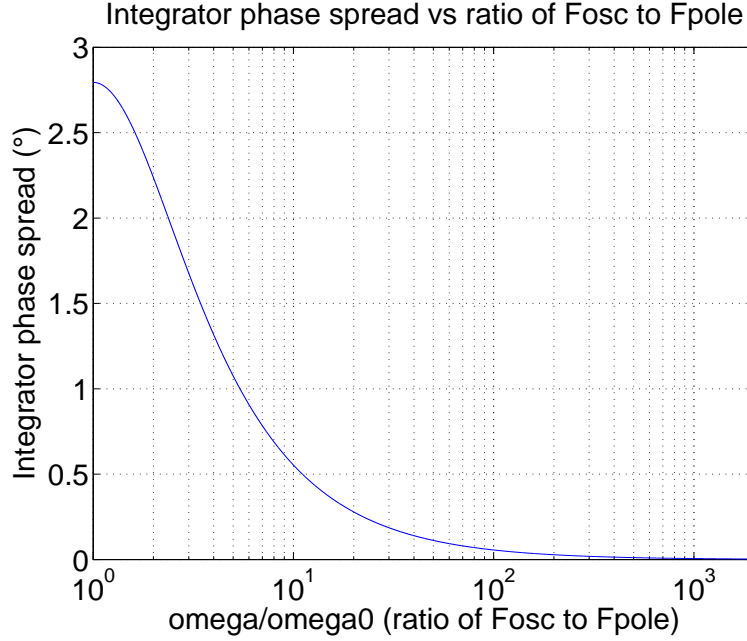
Figure 3.10: This figure shows the phase spread of the integrator versus the ratio between the oscillation and the pole frequency.

Specifications	Value
Z_{in}	$>> R_{tp}$
$V_{n,gm}$	$< V_{n,tp}$
$V_{CM,in}$	0V
$f_{ch,H}$	$> 1\text{kHz}$
$f_{ch,sys}$	1Hz
f_{pole}	$< 44\text{Hz}$

Table 3.1: In this table the specifications for the integrator are shown.

where $\phi_{1,2}$ is the phase delay of the integrator with respectively a 5% higher or lower pole frequency, ω_{osc} is the oscillation frequency and ω_p is the pole frequency. The integrators phase spread is plotted in figure 3.10. The integrator has a negligible contribution ($< 0.01°$) to the total phase delay spread when the ratio between the oscillation frequency and the pole frequency is larger than 550, i.e. the pole frequency is smaller than 44Hz.

The specifications for the electrical integrator are summarized in table 3.1.

Next, the integrator used in [10] is evaluated to check whether it can be re-used in the new design. The architecture of this integrator is a fully differential Gm-C architecture. It consists of a transconductance amplifier and an integration capacitor. The transconductance amplifier, or Gm stage, is implemented by a conventional folded cascode amplifier. Chopping is used to reduce the offset of the amplifier and to modulate the $1/f$ noise out of the band of interest. The output chopping switches are embedded

Specifications	Value
Input pair	PMOS
g_m	22μS
C	130pF
R_{out}	$1.5G\Omega$
f_{pole}	0.5Hz
$V_{os,residual}$	0.8μV
$V_{n,residual}$	17nV$/\sqrt{Hz}$

Table 3.2: In this table the specifications of the used Gm-C integrator are shown.

in the output branches. Figure 3.11 shows the schematic of the amplifier.

The input of the amplifier is at the gates of the input transistors, therefore the amplifier will have a very high input impedance. This ensures that voltage read-out is used.

The input pair of the amplifier is made of PMOS transistors. Using PMOS input transistors facilitates the operation of the amplifier with 0V input common-mode, so it also fits this part of the specifications.

The noise level of the Gm stage is dominated by the noise of the input transistor pair. For this amplifier architecture it is given by 3.9:

$$V_{n,g_m} = 4kT\frac{2}{3 \cdot g_m} = 21nV/sqrt(Hz) \tag{3.9}$$

where k is the Bolzmann constant, T is the temperature in Kelvin and g_m is the transconductance of the input transistor pair, $22\mu S$. The thermopile noise is given by:

$$V_{n,tp} = 4kTR_{tp} = 52nV/sqrt(Hz) \tag{3.10}$$

where R_{tp} is the thermopile resistance, $169k\Omega$. The noise contribution from the thermopiles is almost 2.5 times larger than that of the amplifier and so the noise specification is met.

The folded cascode architecture characteristically has a high output impedance due to the cascode transistors in the output branch. The output impedance of this amplifier was simulated to be $1.5G\Omega$. Together with the relatively large integration capacitor of 130pF the low-frequency pole of the integrator lies at 0.5Hz. This easily meets the specifications. The phase delay spread of the integrator at the oscillation frequency is only 0.0035°, which is 80x smaller than the spread of the thermopiles.

The integrator from the previous work [10] satisfies all the specifications and so it can be re-used in this design. This amplifier has the benefit of being a tested, working design with a robust and simple architecture. The downside of using this architecture is that a relatively large integration capacitor is required to get a low enough pole frequency. This will not be a problem in this design as the dimensions of the chip are determined by the size of the thermopiles. There is plenty of space for the integration capacitor in the center of the chip. The specifications of the integrator are shown in table 3.2.

Figure 3.11: This figure shows the schematic of the chopper amplifier used in the integrator.

3.2.3 Comparator

The system requires a 1-bit comparator to digitize the signal and close the feedback loop. The specifications for the comparator are not stringent, because of the high DC gain of the stage in front of it, i.e. the electrical integrator, attenuates noise and offset. The most stringent specification for the comparator is its speed, since it has to run at a sampling frequency of around 120kHz while being implemented in a mature 0.7μm CMOS technology.

The comparator used in the previous work [10] was simulated to see whether it would function at increased sampling frequency. It is a conventional latched comparator with a pre-amplifier to decrease the offset and kick-back noise. Figure 3.12 shows the schematic of the comparator. The maximum sampling frequency of this comparator is determined by the charging of the voltage at nodes A and B. Ones of these nodes must charge to a voltage higher than 2.5V during the comparators regeneration phase in order for the comparator to make a valid decision. This conditions can be described as:

$$T_{rise} = \frac{2.5}{\frac{\Delta V}{\Delta T}} + T_{propagation} \qquad (3.11)$$

Where $\frac{\Delta V}{\Delta T}$ is the slope of the rising voltage at node A and $T_{propagation}$ is the time between the sampling clock edge and the start of the charging of the nodes A or B. T_{rise} is the minimum time needed to allow the comparator to regenerate properly. The duration of the regeneration phase is half of the sampling period and so the relation
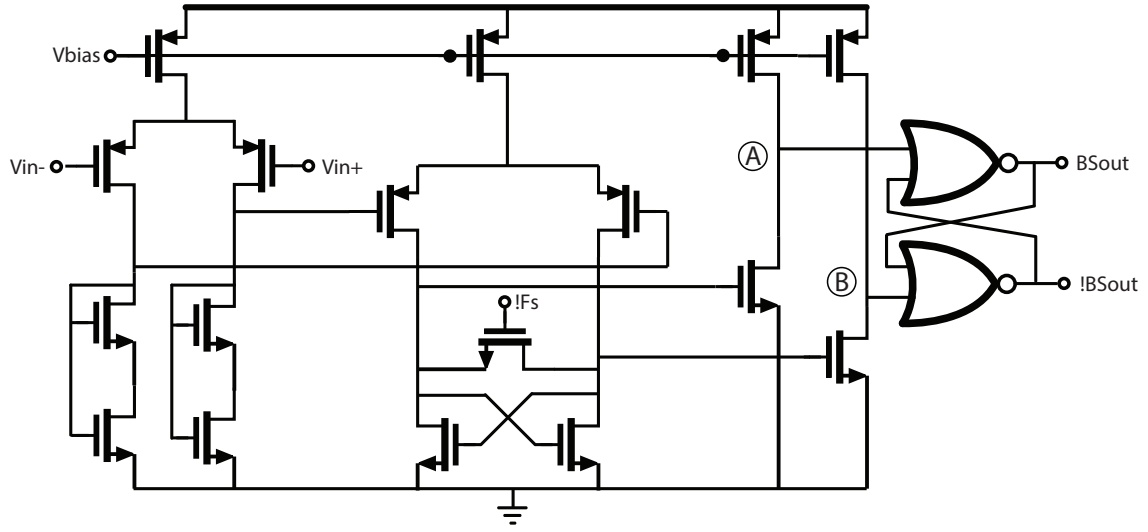
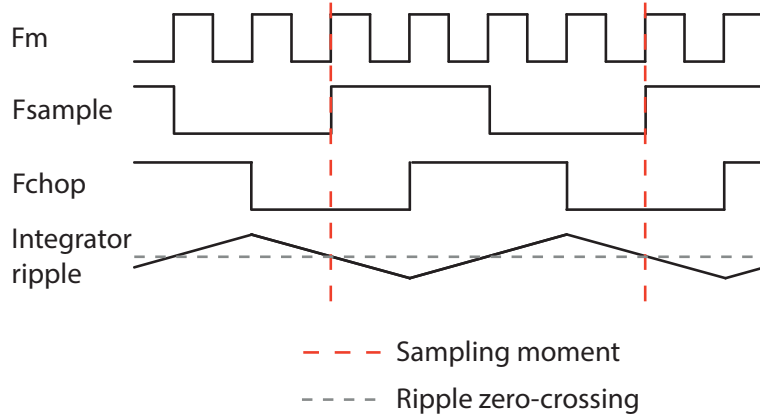Figure 3.12: This figure shows schematic of the comparator.

Figure 3.13: This figure shows the integrator ripple caused by chopping and how it is suppressed by sampling at its zero-crossing.

between T_{rise} and the maximum sampling frequency, $F_{s,max}$, is:

$$F_{s,max} = \frac{1}{(2 \cdot T_{rise})} \tag{3.12}$$

From simulations it was found that the slope of the rising voltage is about 7.5MV/s and $T_{propagation}$ is 120ns. Using this in formulas 3.11 and 3.12, $T_{rise} = 0.45$us and $F_{s,max}$ = 1.1MHz. This is high enough for this design and therefore this comparator was used.

Chopping the G_m-amplifier will produce a triangular ripple on its output voltage. This is suppressed by ensuring that the comparator is sampled at the exact zero-crossings of the ripple. Figure 3.13 illustrates this.
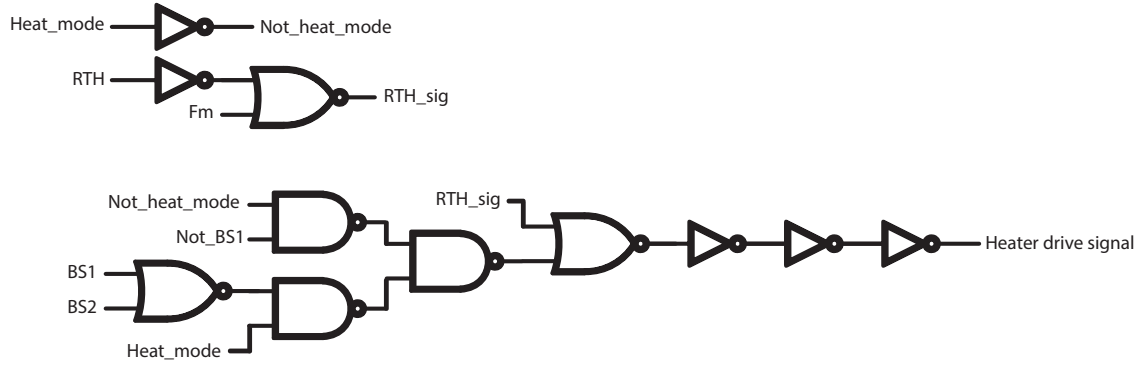
Figure 3.14: This figure shows the schematic of the heater control logic.

3.2.4 Control logic

The heater driving modes described in section 3.1.2 will be implemented by the on-chip logic. This logic will be in the loop and therefore any spread on the delay introduced by this logic will be a source of errors in the conversion. To estimate the magnitude of these errors, Monte Carlo simulations of the circuit were executed. In this section the design of the control logic and the results of the Monte-Carlo simulations will be presented.

The logic will switch between the driving modes based on two static driving signals. The first signal, called RTH, will switch the wind sensor between its normal mode, when low, and the Return-To-Heat mode, when high. The second signal is called heater_mode and will switch the sensor between its normal heater mode (when low) and single heater mode (when high). To accommodate the operation modes the logic shown in figure 3.14 was designed. The circuit consists of several NAND and NOR gates to provide the desired functionality, followed by three inverters of increasing size to drive the large heater driver transistors. On the wind sensor chip, each of the eight heater halves is controlled by its own copy of the circuit. The connections of the signals BS1, BS2 and Not_BS1 are the modulators' bitstreams or their inverse and are for each copy of the circuit determined by the location of the heater.

The influence of the control logic on the accuracy of the temperature measurement was investigated. The propagation delay between a signal change at BS1, which is the output of one of the quantizers, and a change at the heater drive signal will be considered. The spread of this delay will be a source for error in the temperature measurement, as it can be seen as a phase delay. In Montecarlo simulations, two instances of the control circuit were simulated for 100 Montecarlo runs. In figure 3.15 the results of these simulations are shown. The spread of the propagation delay of the first circuit is shown in the left graph. The spread of this delay of the second circuit is shown in the middle graph. To compute the effect of this delay, the difference between these two is calculated and shown in the right graph. The delay difference has a mean value of 185ps and a standard deviation of 8ps. From the time delay difference a phase
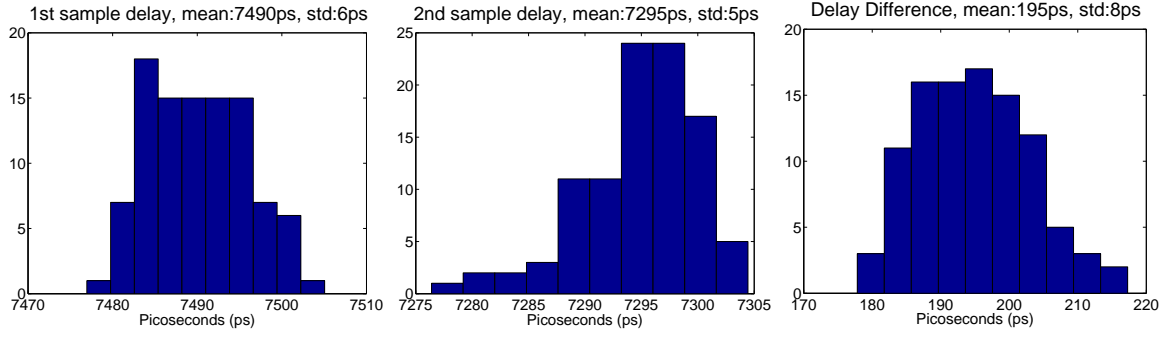
Figure 3.15: This figure shows histograms of the heater control logic Monte Carlo simulations.

delay difference can be calculated via 3.13:

$$\Delta\phi = 360° \cdot f \cdot \Delta t \tag{3.13}$$

Where f is the predicted oscillation frequency, i.e. 1300Hz, and Δt is the time delay difference. The average phase delay difference is calculated to be 0.0865m°. This is very small when compared to the phase error budget of 0.27°, which means that the error caused by the delay of the control logic will be negligible.

3.3 Chip layout

The layout of the wind sensor plays a big role in the actual performance of the wind sensor. However, the effects of the layout on the sensor's operation are quite difficult to simulate. Therefore, no simulation results are presented to support the points made in this section. The influences of the layout, both in the electrical and the thermal domain, are considered qualitatively. The points that will be discussed in the following section are thermal symmetry, clock shielding and signal routing.

3.3.1 Thermal symmetry of bond pads

For the thermal part of the sensor to perform optimally, the sensor should be symmetrical in the thermal domain. Symmetrical in this case means that any thermal disturbance has the same effect on both modulator loops. To obtain thermal symmetry it is important to regard the spacing of the bond pads along the edge of the chip. The bond wires that will be connected to these pads will leak heat away from the sensor and therefore influence the system.

The chip that is developed will be a prototype. It will have three different bond-wire configurations. The different configurations require 8, 12 or 16 bond wires and will accommodate different testing strategies of the chip. Using 8 bond wires is the product mode, in which only the essential pins for operation are wire bonded. The 12-wire configuration is the prototype mode wherein 4 extra pins are bonded out. With these extra pins the different heater driving modes can be selected and the test heater in the North-East corner of the chip can be driven. The 16-wire configuration is the desktop
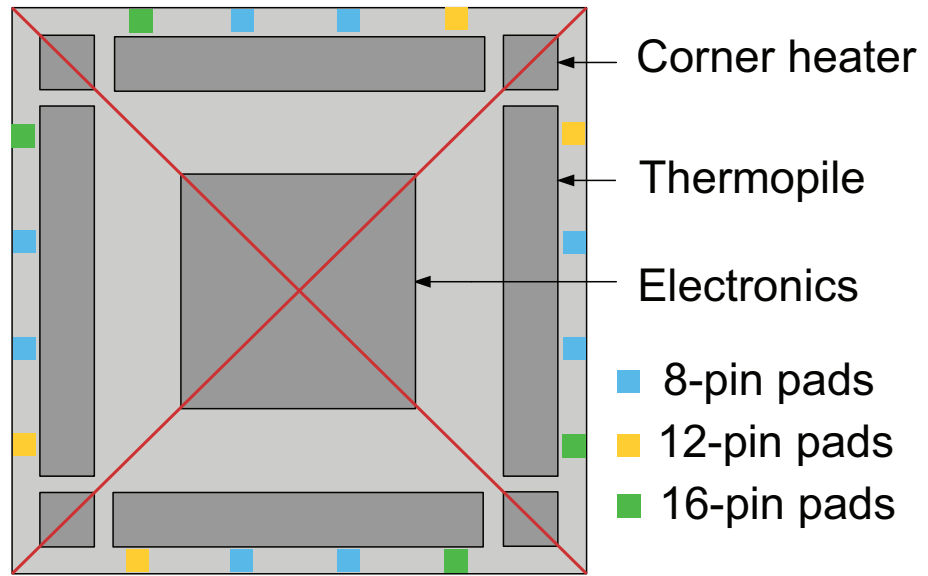
Figure 3.16: This figure shows the bond pad locations and the different bond wire configurations of the chip.

mode. In this configuration the status of the integrators can be checked because the extra pins route the integrating capacitor voltage off-chip.

During the design, it was made sure that in each of these configurations the thermal symmetry would hold. Figure 3.16 shows the spacing of the bond pads. In this figure the bond wire pads for the different configurations are shown by the blue, yellow and green squares. The diagonal red lines show the axis along which the thermal symmetry was assured.

The pins of the wind sensor are listed in table 3.3. In the 8-pin mode only the first 8 pins will be bonded. These correspond to the blue pins of figure 3.16. In the 12-pin mode pins 9 to 12 will be bonded in addition to the pins of the 8-pin mode. They are the yellow pins in 3.16. For the 16-pin mode pins 13 to 16 are also bonded, which are the green pins in 3.16.

3.3.2 Shielded clock lines

Shielded clock lines were implemented in the chip to prevent parasitic coupling from the clock signal to the circuit. In the manufacturing process used, 3 metal layers and one polysilicon layer are available to make interconnects. To implement the shielding on-chip the clock signals were routed in the metal2 layer, fully surrounded by the shield as shown in figure 3.17. The sides of the shield are closed with vias, but they have been omitted from the cross section for clarity. When signals have to be crossed on the chip, the signals are routed to metal1 and the shield to metal2, with vias going to the substrate; the crossing signals pass via metal3. This is shown in the right side of the cross section.

Pin number:	Signal name:
1	Vdd
2	Gnd
3	V_{heat}
4	Gnd_{heat}
5	F_m
6	$F_{Sys.Ch.}$
7	Pol
8	BS_out
9	Heater_mode
10	RTH
11	Vtest-
12	Vtest+
13	Enable_Mux
14	Select_Int
15	Int+
16	Int-

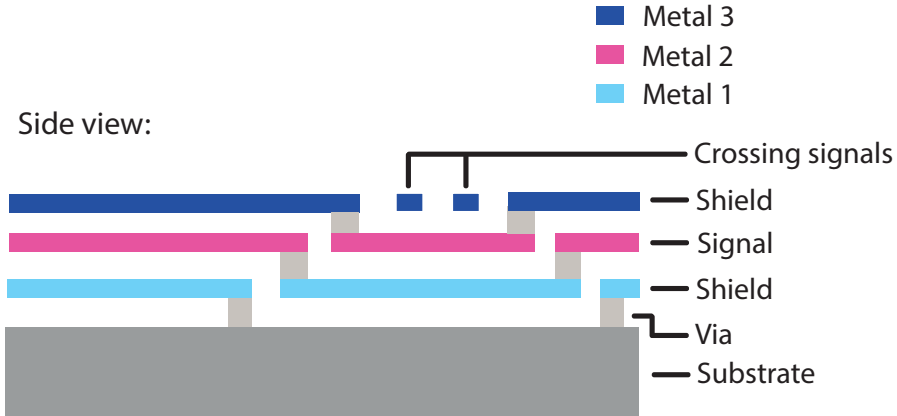Table 3.3: In this table the pins of the wind sensor chip are listed.

Figure 3.17: This figure shows a drawing of the coaxial shield that was placed around the clock signal wires. The vias that close the sides of the shield are omitted for clarity.

3.3.3   Signal routing

The wires connecting the thermopiles to the amplifier are routed around the edge of the chip to keep them as far as possible from any interference. The wires are pretty long (around 4mm) and they add a parasitic capacitance to a very sensitive node, the input of the amplifier. To ensure the capacitance added by the wires is equal for all four thermopiles, the length of each wire is made equal by the addition of a section of dummy wire. Figure 3.18 shows how this was done. The common-mode voltage is 0V, so one side of each thermopile is connected to the ground. This is provided by the shield drawn in black. The shield is similar to the one described in the previous section. It protects the thermopile signals from coupling effects. The other side of the
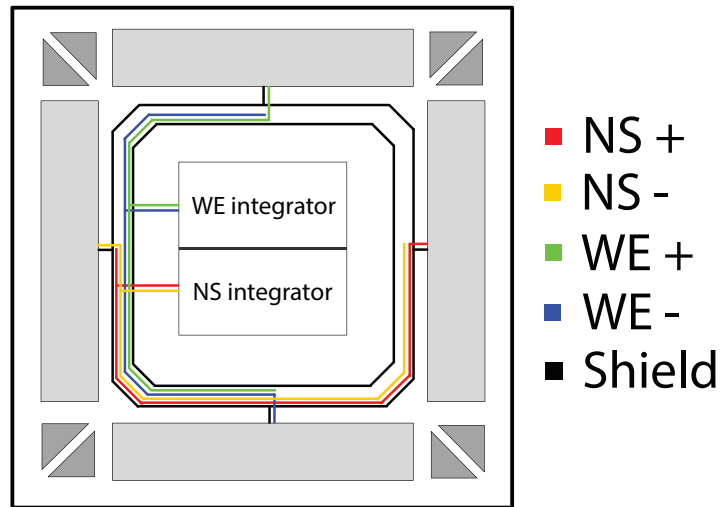
Figure 3.18: This figure shows the routing of the signals from the thermopiles to the amplifier.

thermopile is routed to its respective input terminal on the amplifiers. The dummy wire sections are found at the end of each colored wire on the side opposite to the side of the thermopile they are connected to.

Measurements

4

This chapter describes the two test setups that were developed to measure the performance of the wind sensor chip. The first test setup utilizes the test heater in the North-East corner of the chip to create a controlled thermal imbalance in the chip in a desk-top environment. This setup is used to find the optimal operating point of the sensor, i.e. the optimum sampling frequency and heater power, without having to use a wind tunnel. The second test setup is used to measure the actual wind sensing performance of the chip in a wind tunnel.

First the design of both measurement setups and the measurements for which they were used will be discussed. Afterwards the interface that was developed to drive the sensor is described. The results of the measurements and the wind sensing performance of the sensor are then discussed, after which chapter concludes with a performance comparison table.

4.1 On-desk setup

To find the optimal operating point of the sensor chip, a test setup was developed to evaluate the performance of the wind sensor without a wind tunnel. This setup is used to evaluate the resolution and linearity of the sensor's electronics. The chip was bonded in a ceramic DIL-package to speed-up the testing process. While this package does not appear to be very similar to the actual wind sensor package, it was later verified that the performance of the chip in this package was similar to its performance in the wind sensor package and so the results obtained with the desk-top setup are assumed to be valid for the wind sensor package.

The noise introduced by the electronics is measured by measuring the noise on the sensor's output while there is no wind present. To measure the linearity of the sensor, the on-chip test heater in the North-East corner is used to create a controllable thermal imbalance. By measuring the sensor's reaction to this its linearity can be determined. Exposing the chip to wind would also create a thermal imbalance and therefore it can be expected that the linearity measured in this experiment is representative of the sensor's linearity when exposed to wind.

During these measurements, it is critical that the sensor is exposed to no actual wind or air flow. Therefore the sensor was placed in a small air-tight box. To further stabilize the environmental conditions of the sensor chip during long measurements an aluminum block was fixed to its package.

In figure 4.1 a drawing of the on-desk setup is shown. The sensor chip is driven by a PCB which is connected to a PC via a National Instruments USB6259 data-acquisition (DAQ) card. This card is controlled by a Labview program that was developed to operate the sensor in such a way that its performance at various settings can be evaluated.
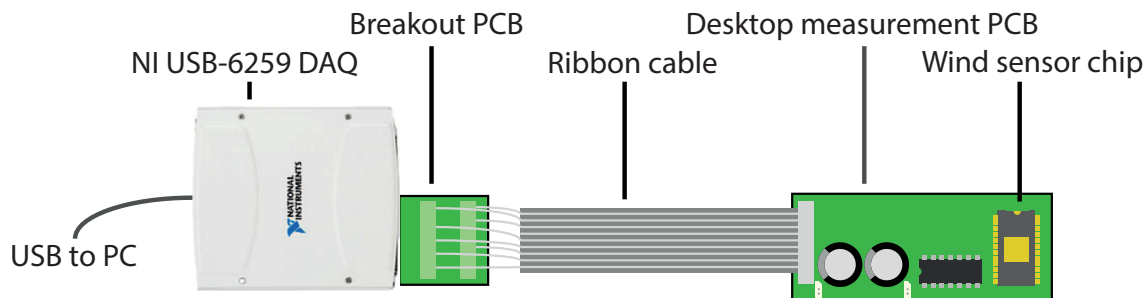
Figure 4.1: This diagram shows the setup used in the desktop measurements.

There are two high-current voltage followers on the PCB, which supply the current to the test heater and the system heaters and are controlled by an analog voltage coming from the DAQ card. By varying the voltage V_{heat} the reference power for the system P_{ref} can be varied. As the power dissipated in the heaters is much higher than any other power dissipated in the chip, this should be as low as is possible while maintaining performance. By varying the voltage V_{test} the amount of power dissipated in the test heater and thus the thermal imbalance can be controlled. This is used to evaluate the linearity of the thermal balancing loops.

4.2   Wind sensor setup

After the correct operating point was found, the chip was tested in a wind tunnel to measure its actual wind sensing performance. The wind sensor was exposed to wind with speeds between 1 and 25 m/s from all angles in order to quantify the errors in the wind speed and direction.

For the sensor chip to be properly exposed to the wind, but not to the environment, a special wind sensor package has been developed [14]. In this package the chip is glued on the back of a ceramic plate that is exposed to the wind and thus not in direct contact with the wind but only in thermal contact. This package also ensures that the flow is always turbulent around the sensor chip and makes the system less dependent on the incoming angle of the wind with respect to the chips horizontal plane. A cross-section of the package is shown in figure 4.2.

To test the sensor in a wind tunnel a set of two PCBs had to be designed; the Wind Sensor PCB which is located in the wind sensor enclosure and the Transceiver PCB which is located near the DAQ card. These PCBs allow the sensor to be connected to the DAQ card with a 10 meter long cable. All data and power will be transferred over this cable. A readily available UTP cable was chosen as the cable. It contains 4 twisted pairs of wire. The 3 signals can be sent differentially over 3 pairs; the final pair can be used to supply power and ground to the chip. Using twisted pairs minimizes cross-coupling between the signals and minimize the effect of external electromagnetic interferences.

The Wind Sensor PCB has to create the supply voltages for the wind sensor chip and facilitate the communication between the chip and the other side of the cable. It has to be small enough to fit inside the wind sensor enclosure. A photograph of the
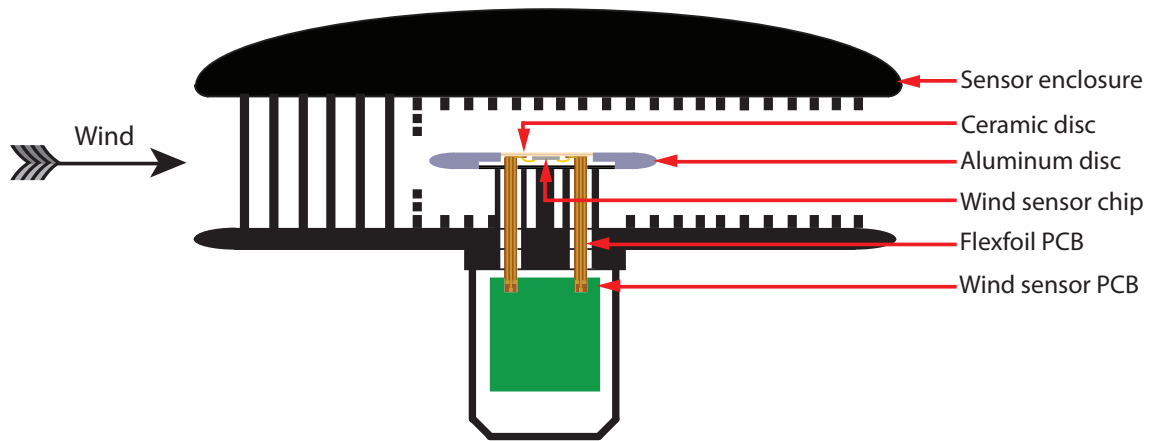
Figure 4.2: This diagram shows a detailed cross-section of the wind sensor package.

Wind Sensor PCB, connected to the sensor chip is shown in figure 4.3. The PCB is 28mm wide and 37mm long.

The Transceiver PCB will be a buffer between the cable and the DAQ for the signals and will also connect the power supply to the cable. The signals that have to be sent to the chip are the clock and the low-frequency chopping clock; the chip will send its bitstream output back to the DAQ. Furthermore, power and ground need to be supplied to the chip. A photograph of the Transceiver PCB is shown in figure 4.4. The PCB is 28mm wide and 36mm long.

On each PCB there is a LDO regulator to create a 5V supply. The supply voltage on the UTP cable will be 7V to allow a little voltage drop. On the wind sensor PCB there is another LDO with a variable voltage output that can be set with a potentiometer to tune Vheat and thus the reference power. Finally on the wind sensor PCB there are two jumpers with which the operating mode of the sensor chip can be set and a header of soldering pads which can be easily soldered to the flexible PCB that connects the Wind Sensor PCB to the chip.

The total measurement setup is shown in figure 4.5. A detailed block diagram of the setup is shown in figure 4.6.

4.3   PC interface

To provide a flexible interface between the wind sensor test setups and a PC a National Instruments USB6259 data-acquisition card was used. This is a highly flexible device which connects to a PC over USB and contains a lot of digital and analog inputs and outputs. This DAQ card also has two hardware counters which are employed as clock dividers to ensure that the clock signals sent to the chip are very well defined. The DAQ card is controlled via a Labview program that handles the proper set-up of the sensor and converts the data it acquires to the NS and EW bitstreams or to the bitstreams' decimated values, depending on what measurement mode is selected. The output of this program is then processed in MATLAB to obtain the results of the measurement.
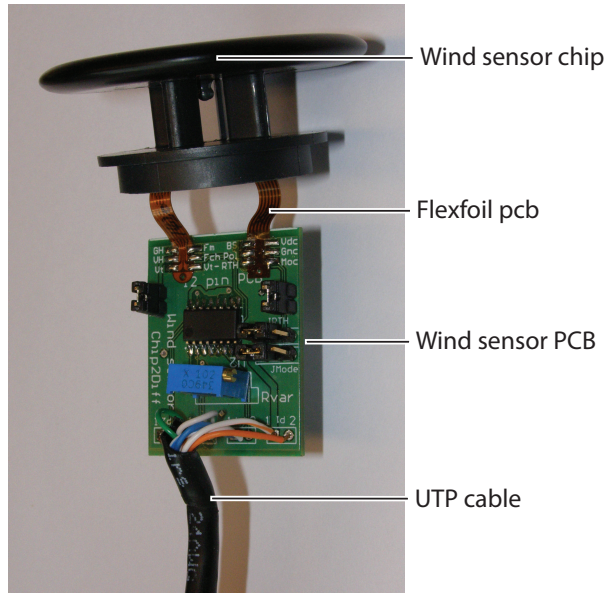
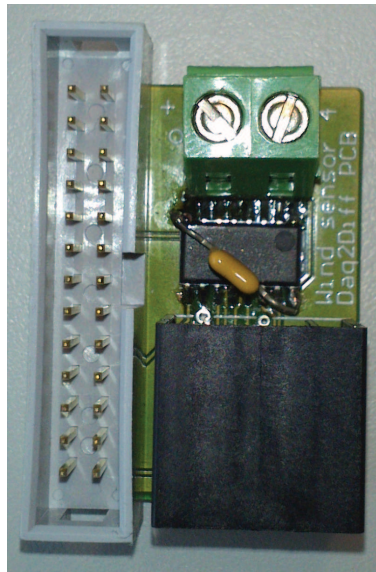Figure 4.3: A photograph of electronics inside the wind sensor enclosure.

Figure 4.4: A photograph of the Transceiver PCB.

4.4 Results

The two setups that are described in the previous sections were used to measure several performance aspects of the wind sensor chip. In this section the results of the measurements will be presented. First the results from the on-desk measurements will be shown and then the results from the measurements in the wind tunnel will be shown.
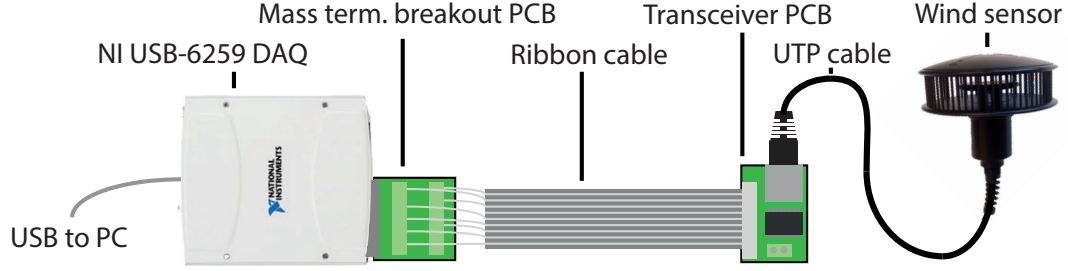
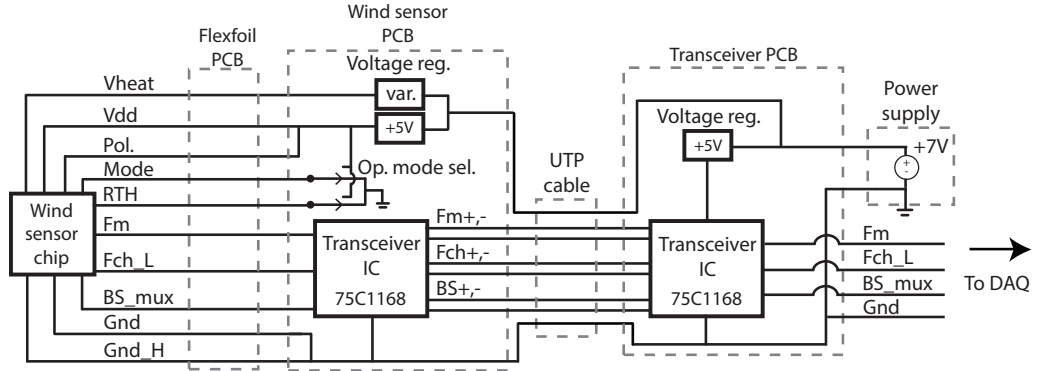Figure 4.5: This diagram shows the setup used to measure the performance of the wind sensor in a wind tunnel.

Figure 4.6: This is a block diagram of the setup used in the wind tunnel.

4.4.1 Desktop measurements

The on-desk setup is used to find the operating point for the wind sensor. This operating point includes the sampling frequency, an amount of reference power, i.e. heater power, and a heater driving mode at which the sensor performs best. First the minimum level of the reference power will be determined by considering the output range of the sensor and the oscillation of the system. Next the sampling frequency will be determined by again checking the oscillation and by measuring the noise performance. Finally the linearity of the sensor will be evaluated for each heater driving mode.

The reference power must be high enough so that both modulators oscillate while exposed to wind with a speed in the range of 1 to 25m/s and from any angle. This means that the residual offset that is present in both modulators plus the wind-induced output value must stay well within the modulators references. The behavior of the wind sensor chip for different amounts of reference power was investigated. Figure 4.7 shows the measured offset of the modulator, i.e. its output value when there is no wind present, versus the total heating power dissipated in the chip. The offset is larger for lower heater powers. Above 75mW of heater power, the offset keeps constant with the increase of heater power. In [10], the sensor used only a small portion of its dynamic range. The output of the sensor stays within -0.25 and +0.15 when exposed to wind speeds under 25m/s. The new sensor will similarly only use a small portion of its total range (when operated in normal mode) and so the signal plus offset will fit in the
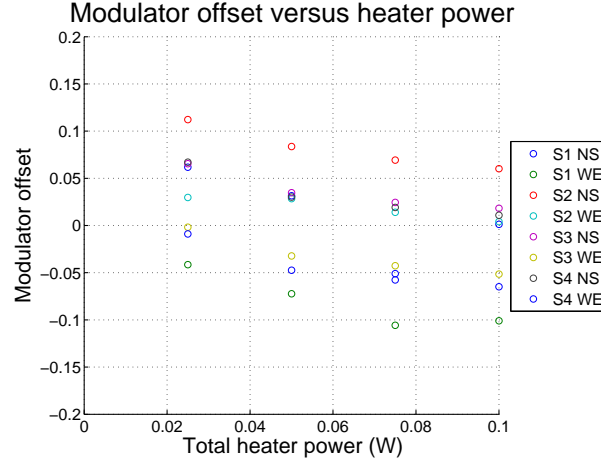
Figure 4.7: This graph shows the offset of the NS and EW modulator for four sensor samples versus the total power dissipated in the heaters.

modulators range for all heater powers that were tested.

A second criterion for setting the amount of heater power is the system's oscillation. With too little heater power the system will not oscillate and therefore not function properly. To quantify this effect the output bitstream for heater powers varying from 3 to 62mW was measured and a Fast Fourier Transform (FFT) of the output bitstream was calculated. The sampling frequency was set at 200kHz for these measurements and each was 1 second long. Figure 4.8 shows the resulting frequency responses. For very low heater power the system does not show the desired oscillatory behavior. For heater powers above 22mW the FFT of the bitstream shows a well-defined peak at the oscillation frequency, around 1250Hz, which agrees with the expectation presented in section 3.1.1.

The effect of varying the sampling frequency on the oscillation of the system was also measured. This was done by setting the heater power at its maximum, 130mW, and then varying the sampling frequency from 2.5kHz to 250kHz. An FFT was applied to the output bitstream from a 1 s measurement and the results are shown in figure 4.9. This figure shows that the oscillation frequency of the system is dependent on the sampling rate when this is below 150kHz. The sampling frequency must be set higher than 150kHz to operate the sensor properly. This is confirmed by figure 4.10, in which the main oscillation frequency of the system is plotted against the sampling frequency. From Fs larger than 150kHz, the sampling frequency is almost constant around 1255Hz. The thermal time constant of the system then dominates the time constant of the entire system, which is desirable for the temperature measurements. The residual variation of the oscillation frequency corresponds to less than 0.5°C of temperature variation, which is caused by room temperature variations during the measurement.

To check the noise-performance of the chip the noise in the bandwidth from 0 to 100Hz (corresponding to the first 100 FFT-bins) is computed and plotted versus the sampling frequency in figure 4.11. The graph shows that the noise content of the output bitstream rises very steeply for very low sampling frequencies and settles to stable value
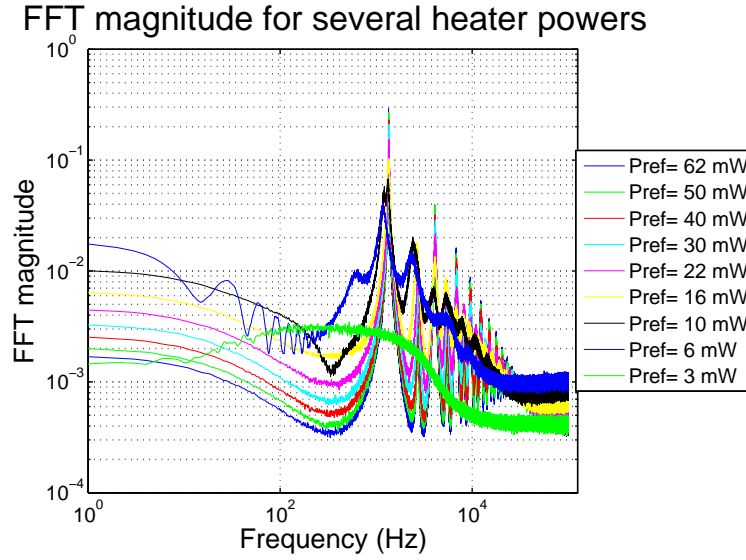
36

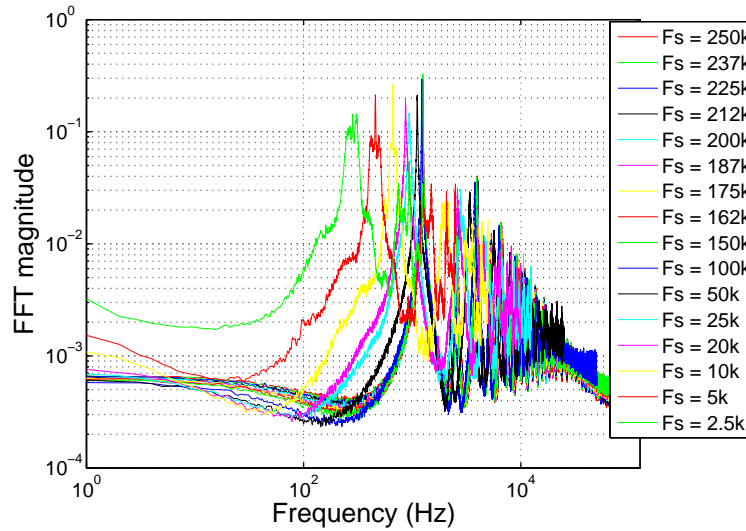Figure 4.8: This graph shows FFTs of the modulator's output bitstream for heater power ranging from 3 to 62mW.

Figure 4.9: This graph shows FFTs of the modulator's output for sampling frequencies ranging from 2.5 to 250 kHz.

for Fs>20kHz. This requirement is less stringent then the result obtained by checking the oscillation of the system. Another experiment was also performed in which the noise on the decimated output value was measured for 160 different levels of test heater power between 0 and 16mW. At each point 100 1-second conversions were made; the standard deviation was then calculated for these 100 data points. For this experiment the sampling frequency was set to 120kHz and the heater power to 25mW. Figure 4.12 shows the results. The standard deviation is smaller than 0.00035 for all test heater input powers.
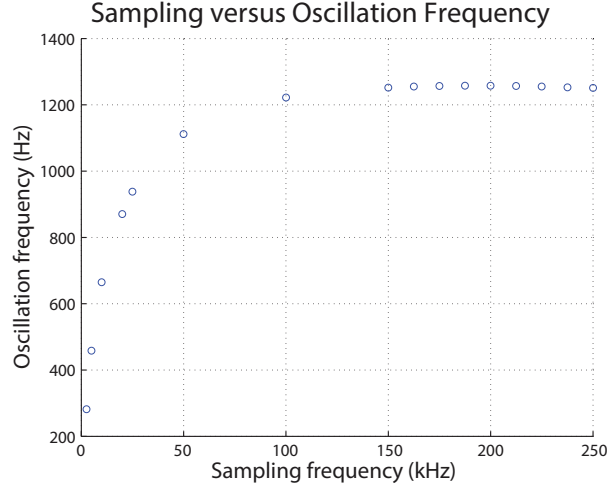
Figure 4.10: This graph shows the measured oscillation frequency of the output versus the sampling frequency.
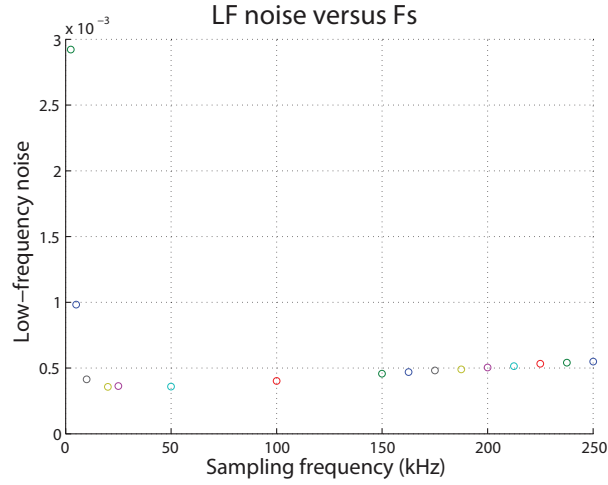

Figure 4.11: This graph shows the measured noise level of the output versus the sampling frequency.

The SNR of the total system can be calculated with formula 4.1:

$$SNR = 20^{10} \log(\frac{1}{\sigma}) \tag{4.1}$$

In this equation σ is the noise on the output value, i.e. standard deviation from figure 4.12. The SNR is calculated to be 69dB.

As was shown in section 2.3 the modulator needs to be linear to at least 7.9 bits to digitize the angle of the incoming wind with an error smaller than 1°. The linearity of the modulator was measured in normal, RTH and 1H mode. The sensor was operated at Fs=120kHz and Pheat=25mW in normal mode, at Fs=120kHz and Pheat=37.5mW in RTH mode and at Fs=120kHz and Pheat=25mW in 1H-mode. These settings make
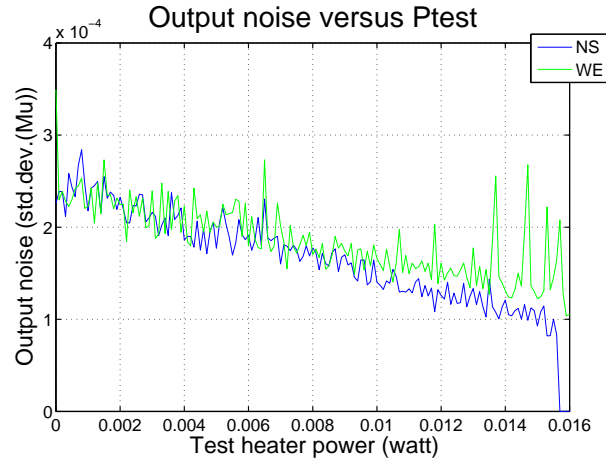
Figure 4.12: This graph shows the noise level of the output versus test heater power.
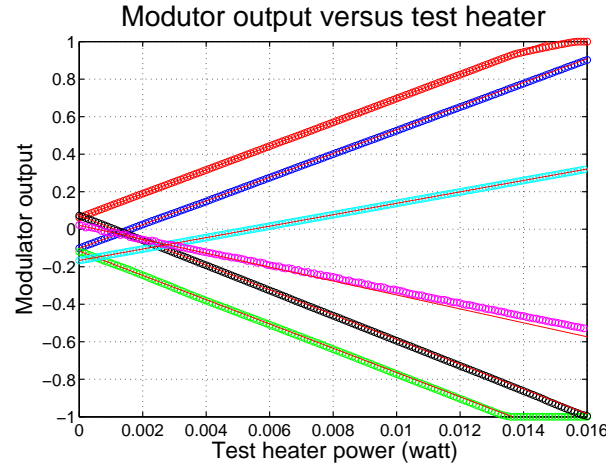

Figure 4.13: This graph shows the output of the sensor versus the test heater power in normal, RTH and 1H modes.

the differential power of the modulators the same for normal and RTH modes, which results in equal sensitivity to power dissipated in the test heater. In 1H mode, the total heater power should be set to 12.5mW to achieve the same sensitivity. This means that in normal mode half of the heater power is common-mode. The sensor still requires at least 25mW to oscillate properly and so the heater power is set to this value, which results in a 2x lower sensitivity. The test heater power is swept from 0 to 16mW in 160 steps. At each point 100 samples of the wind sensor output were averaged to assure the noise in the measurement was negligible. Figure 4.13 shows the outputs of the sensor for each of the operating modes, together with a fitted, straight, red line through the data points. The red and black points show the output of the NS and EW modulator in normal mode. The blue and green points show the NS and EW output values in RTH mode. The cyan and magenta colored points show the output in 1H mode. As expected, the sensitivity of the system in 1H mode is 2x lower then in the other modes.
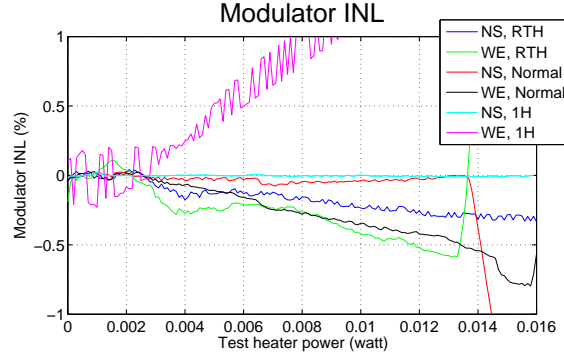
Figure 4.14: This graph shows the nonlinearity of the sensor with respect to power dissipated in the test heater.

The Integral Non-linearity (INL) of the sensor is defined as the deviation of the sensors input-to-output curve from a straight line; its value is found by fitting a straight line through the data and then calculating the percentual difference between the fitted line and the actual output values. It is shown in figure 4.14. The INL is slightly worse in RTH mode than in normal mode, but it is still smaller than 0.3% in the part of the sensors dynamic range that is used during wind measurements; this means that modulator satisfies the linearity condition of 7.9 bits. In 1H mode, the EW modulator does not satisfy the linearity requirement, while the NS INL is very small. This suggests that the 1H mode actually does not function properly and therefore it was not used in the following wind tunnel tests.

From these experiments it can be concluded that a good operating point for the wind sensor is a sampling frequency of 120kHz and a heater power of 25mW. The performance of the sensor was measured in a wind tunnel and the results from these measurements are shown in the next section.

4.4.2 Wind tunnel measurements

Preliminary measurements were done with 25mW of heating power and at a sampling frequency of 120kHz. The effect of operating the sensor in RTH mode was investigated at this operating point. The wind sensor was exposed to wind speeds of 1, 4, 9, 16 and 25m/s from 12 equally spaced angles. As can be seen in figure 4.15 the average output of the modulators is a sinusoidal function of wind direction, whose amplitude is a monotonic function of wind speed. When the sensor is operated in RTH mode, the amplitude of the sinusoidal functions is 3x larger than in normal mode, i.e. the sensor is 3x more sensitive to thermal imbalances caused by the wind. The measured data is used to compute the coefficients for the calibration model that was discussed in section 2.3. Equations 4.2 and 4.3 show the model equations again.
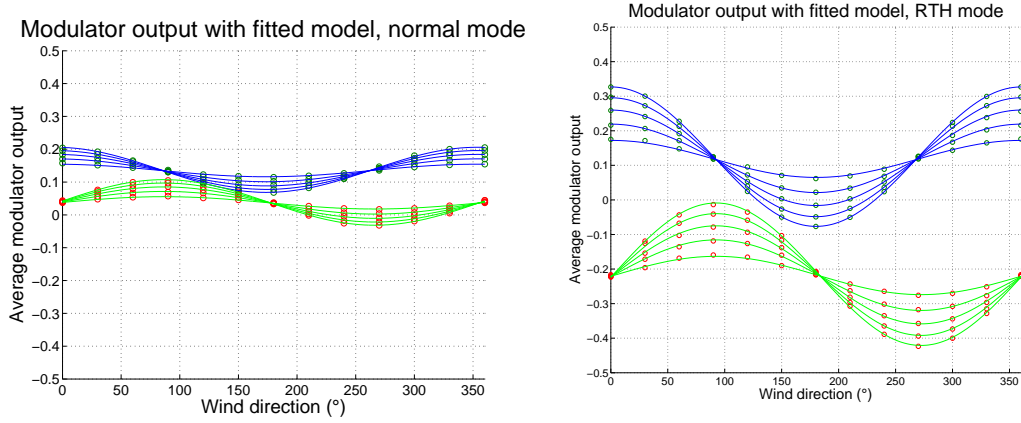
Figure 4.15: Graphs showing the measured output values of the wind sensor in normal and RTH modes.

$$\mu_{NS} = (\frac{\sqrt{U}}{A_{NS} + \sqrt{U} \cdot B_{NS}}) \sin(\theta + \delta_{NS}) + \sqrt{U} \cdot D_N S + E_{NS} \qquad (4.2)$$

$$\mu_{EW} = (\frac{\sqrt{U}}{A_{EW} + \sqrt{U} \cdot B_{EW}}) \cos(\theta + \delta_{EW}) + \sqrt{U} \cdot D_{EW} + E_{EW} \qquad (4.3)$$

With the calibrated model and the measured data the accuracy of the sensor was determined. Figure 4.16 shows the error plots for one of the sensors for 5 wind speeds from 12 angles, for both normal and RTH modes respectively as blue □'s and green ○'s. Each line of the plots shows the error of the sensors at one wind speed. The middle graph shows the relative speed error from the sensor. A relatively large error of around 30% is measured at 1m/s wind; for the other wind speeds the error is smaller than 9%. The left graph shows the absolute speed error of the sensor; the error is smaller than 0.7m/s in all cases. The large relative speed error at 1m/s is small when viewed in the absolute sense and thus not a problem. The right graph shows the wind angle measurement error of the sensor. This measurement is also worse for wind speeds of 1m/s with an error of $\pm 6°$ instead of $\pm 3.5°$ at higher wind speeds in both modes. As can be seen in the graphs, using RTH does not improve the accuracy of the sensor. It does increase the part of the sensor's dynamic range that is used in wind measurement, which increases the SNR. Equation 4.1 can be modified to take this into effect:

$$SNR = 20^{10} \log(\frac{\mu_{max}}{\sigma}) \qquad (4.4)$$

Where μ_{max} is the maximal signal measured and σ is the noise measured. μ_{max} is measured to be 0.15 in normal mode and 0.4 in RTH mode; σ is measured to be around 0.0004 in both modes. This results in an actual SNR of 51dB in normal mode and 60dB in RTH mode. The overall performance observed was not as good as was expected; a second set of measurements was done with increased heater power to see if this was the limiting factor in these measurements.
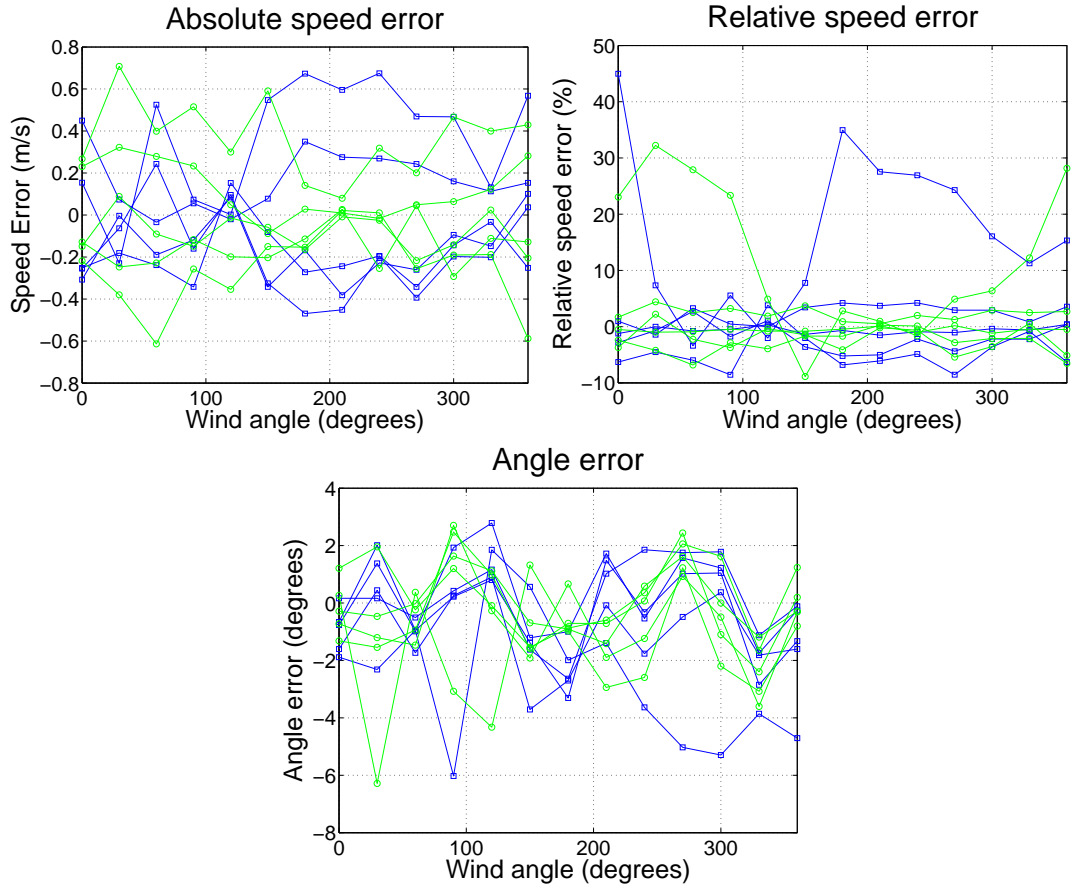
Figure 4.16: These graphs show error plots of the preliminary measurements for normal mode (blue, □) and RTH mode (green, ○).

For the second set of measurements four sensors were measured in order to get an indication of the spread between the sensors. Both the heater power and sampling frequency were increased for the second measurements. The heater power was set at 50mW and the sampling frequency was set to 150kHz. The use of RTH did not improve the accuracy in the previous measurements and so the sensors were operated in normal mode.

Figure 4.17 shows the error plots of one sensor from the second set of measurements; the other 3 samples achieve comparable performance and their error plots are included in Appendix A. In these plots the red line shows the error a wind speed of 1m/s and the black lines show the measurements at the higher wind speeds. The performance is a bit better than the performance observed in the preliminary measurements. The relative speed error is dominated by a large error from the measurement at 1m/s with a maximum value of 25%, but is smaller than 7% for the other wind speeds. The absolute speed error is smaller than 0.6m/s and the angle measurement error is smaller than ±6° for 1m/s and smaller than ±2° for higher wind speeds. The loss of accuracy at low wind speeds is attributed to a loss in sensitivity compared to the previous work, due to the altered temperature profile created by changing the heater positions with
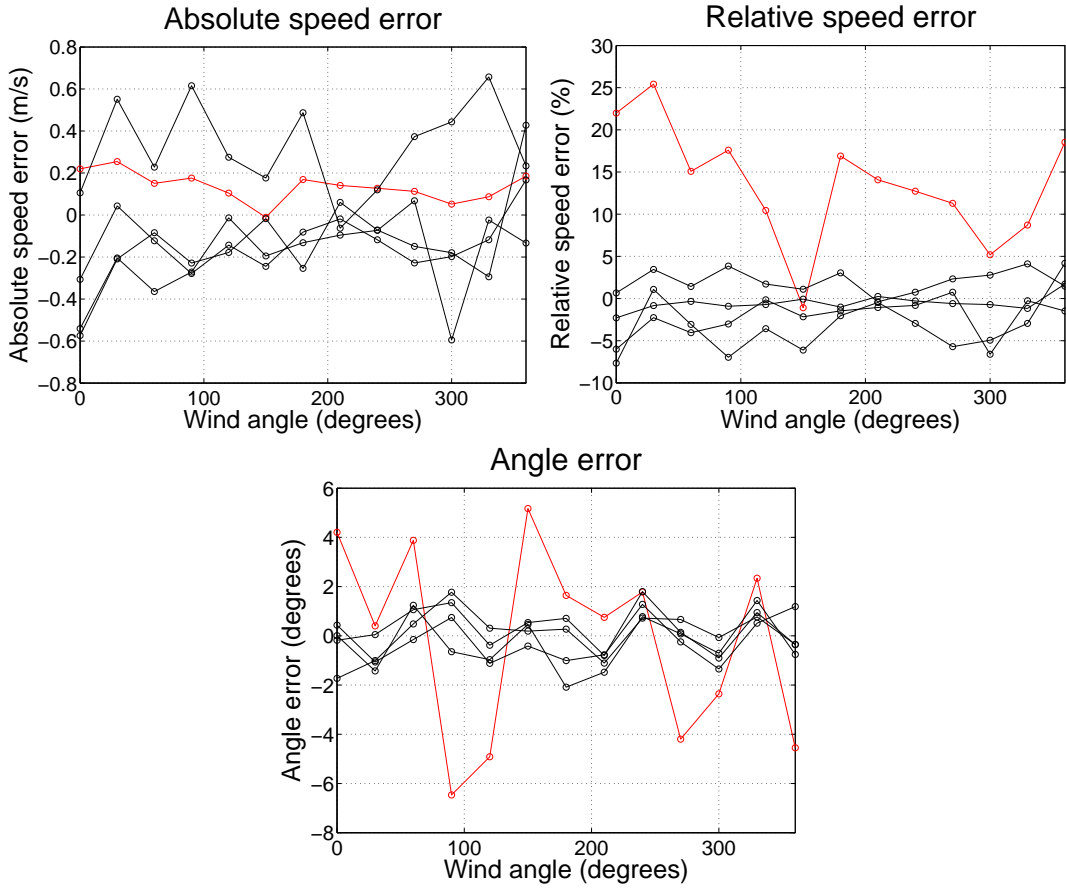
Figure 4.17: This graph shows error plots of the definitive measurements for one sample.

respect to the sensing thermopiles. This was confirmed by a recent publication, where the effect of the placement of the heaters to the sensitivity of the sensor was researched [15]. This paper shows that the thermal gradient experienced by the thermopiles is larger if the heaters are placed inside the ring formed by the thermopiles.

The spread of the calibration coefficients for four sensors was investigated. Table 4.1 shows the average value of these coefficients and their spread. Between the four measured sensors, the gain coefficients A and B vary about 8% and so an accurate determination of these is necessary. This means that the wind sensor will still need an elaborate calibration. The coefficient δ is the angle offset between the sensor and the measurement setup. This is static for each measurement and determined by the placement of the sensor. Its spread is irrelevant to the performance of the sensor. Unlike in the previous work[10, 6] the offset present in the modulator output is quite constant over wind speed, i.e. D is very small compared to E. Due to this a simplification of the calibration procedure might be possible, but it has not yet been performed with good results and so it will not be discussed further.

43

Calibration	NS Modulator		EW Modulator	
coefficients	Avg. value	Deviation*	Avg. Value	Deviation*
A	51.0626	8.91	50.1879	9.42
B	4.3981	0.909	4.3708	0.401
δ	1.6120	0.155	-1.5625	0.174
D	2.6e-4	14.8e-4	-9.05e0-6	5.28e-4
E	0.0027	0.111	-0.0466	0.0516

Table 4.1: This table shows the average value and the deviation of the calibration model coefficients.
*=This is the [Max.-Min.] deviation, calculated by subtracting the smallest value from the largest value found.

4.4.3 Temperature measurements

The temperature measuring capabilities of the wind sensor were measured in a temperature-controlled oven. As explained in section 2.4, the wind sensor can be used as a temperature sensor by measuring the oscillation period of the output bit-streams. The operating point of the wind sensor for this measurement is Fs=60kHz and Pheat=25mW. The chip, in the wind sensor package, was attached to a aluminum block which contains a Pt100 temperature sensor. The sensor was exposed to temperatures ranging from -40°C to +50°C in steps of 10°C. At the different temperatures the oven was given time to let the temperature of the metal block, as measured by the Pt100, stabilize to within 0.005°C of the set temperature. In order to reduce the effect of noise in the results, 100 1-second measurements were done at each point and the results were averaged. The RMS noise observed in these measurements was about 1°C. This is a significant increase in noise compared to the prior work which may be cause by the lowered oversampling ratio (OSR), i.e. the ratio between the sampling frequency and the oscillation frequency. In the prior work this was about 500 and in this work it is around 50.

Four sensors were measured to see whether with a simple batch calibration and a one-point trim, a reasonable accurate temperature measurement can be achieved. The effect of the temperature on the oscillation period of the four measured sensors is shown in figure 4.18. From this graph the sensitivity of the systems oscillation period to temperature,relative to its oscillation period at 0°C, can be calculated via:

$$S_{relative} = \frac{\frac{\Delta\tau}{\Delta T}}{\tau_{0°C}} \tag{4.5}$$

In this formula τ is the oscillation period of the output at a certain temperature T. Taking Δ as the difference between the measurements at -20°C and +20°C, the relative sensitivity is calculated to be 0.0041/°C, which is only 15% higher than the relative sensitivity of [10], 0.0036/°C.

A batch calibration was performed with the data of the four sensors and their respective temperature measurement errors were determined. The results are shown in figure 4.19. The largest error measured is 2.6°C. The spread between the sensors is too large without further calibration.
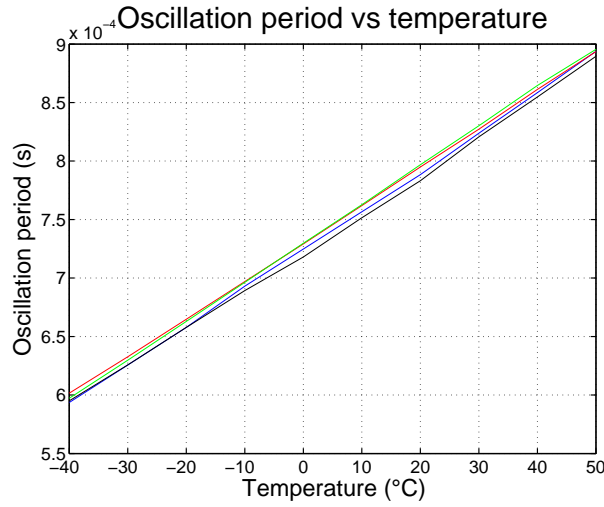
Figure 4.18: Graph showing the measured oscillation period of the sensors versus temperature.
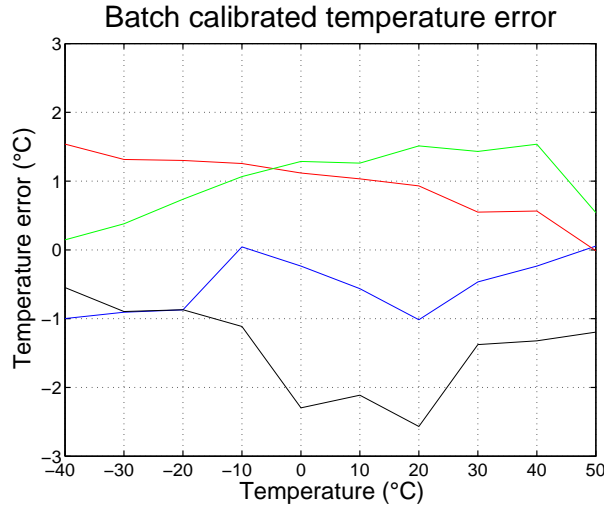

Figure 4.19: Graph showing the error in the temperature conversion after batch calibration.

A 1-point offset trim was then applied at 20°C, which is easily realizable because it is close to room temperature. After this trimming operation the measured temperature errors were again calculated and plotted in 4.20. The maximum error for all four sensors is now reduced to ±1.3°C. The graph shows that a more extensive trim will produce better results, because the plotted errors per sensor have different slopes. Each extra trimming point represents a significant increase in cost and for this sensor more than 1 trim point was not deemed viable and not further investigated.

To verify that the performance of the sensor in these measurements is not limited by the sampling frequency of 60kHz, two sensors were also measured at 120kHz. Figure 4.21 shows the oscillation period of the two measured samples, for the measurements at both sampling frequencies. The graph show that increasing the sampling frequency increased the oscillating frequency, but does not decrease the spread between the sen-
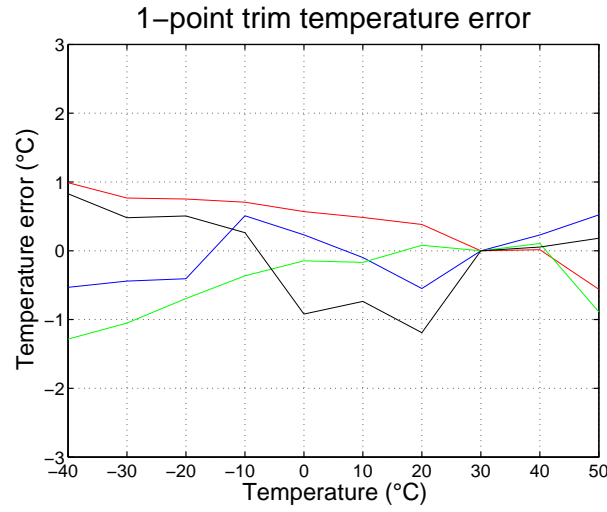
Figure 4.20: Graph showing the error in the temperature conversion after batch calibration and a 1-point trim.
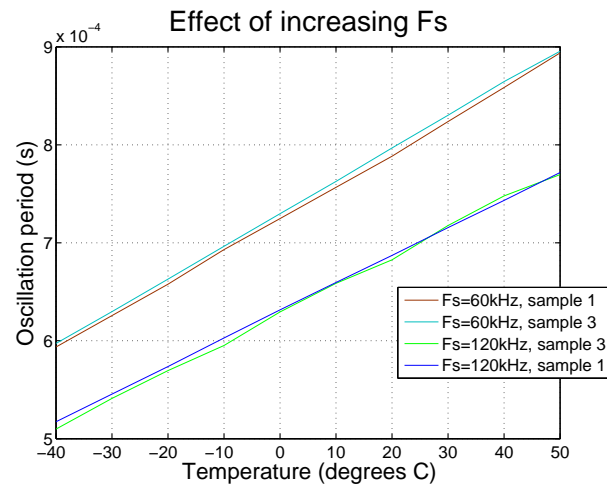
Figure 4.21: Graph showing the effect of increasing the sampling frequency on the oscillation period over temperature.

sors. The batch calibrated temperature accuracy, calculated from the data in this plot, does not show an improvement from the increased sampling frequency. The RMS noise of these measurements was still about 1°C.

A temperature accuracy of 0.1° C was set as the initial goal for this design. During the design phase it became clear that this was unachievable with the thermopile/heater configuration of this sensor, since the spread of the thermopiles alone consumes the entire phase budget. However, the phase delay spread for the other components of the circuit were estimated to be so small that it was expected that the accuracy would be close to the specified value. The measured accuracy deviates a lot from this and so it is probable that an extra source of phase delay was not considered, e.g. that the

comparator is actually not quite fast enough. Another reason that may have caused the loss of accuracy is that the measurement is limited by the high noise caused by the accompanying loss of OSR.

4.5 Performance comparison

In this section the measured performance of the wind sensor presented in this thesis will be compared to several other works. First, it is compared to the work of J. Wu [8], which served as a basis for the design of the new wind sensor. It is also compared to the recent work of Y. Zhu[15], which describes a MEMS thermal wind sensor.

The wind sensor presented in [8] consists of a chip made with a conventional $0.7\mu m$ CMOS technology which is placed in a special enclosure, just as the design in this work. On the chip, two loops cancel thermal imbalances in the North-South and East-West directions by activating heaters on the appropriate side of the chip. In [8] to idea was presented to add an integrator to the thermal balancing loop to create a second order thermal sigma-delta. With this addition this sensor can operate with only 25mW of heater power and can also function as a temperature sensor. However, the temperature measurements is very slow due to the low oscillation frequency (around 30Hz) of the system. Compared to the new sensor, this design is a bit more accurate. The wind measurement accuracy of that sensor is 4% in speed and 2° in angle. Its temperature error after batch calibration is $\pm 1°$C. The RMS temperature noise it achieved is smaller at $\pm 0.15°$C versus $\pm 1°$C for the new design. It does require a substantially longer temperature measurement time of 8 seconds. Furthermore, the decimation filter in [8] is a tracking $sinc^2$ filter, which is more complex than the fixed-length $sinc^1$ used in this work. The sensor requires the connection of 12 bond wires to the chip.

The sensor presented in [15] is a MEMS-based thermal wind sensor. The sensing part of the system is a central heater with several thermistors around it. These are constructed on a silicon-in-glass(SIG) substrate. The SIG substrate is constructed so that its thermal conductivity is anisotropic, which enables a low power consumption of just 25mW. The substrate thickness and the size and placement of the heaters and thermistors are optimized based on simulation results in order to optimize the sensitivity of the sensor. The read-out electronics are located on an external PCB. The circuit consists of two discrete instrumentation amplifiers and two ADCs on-board a microprocessor. The sensor has an angle accuracy of 6°and a speed accuracy of 2.5%. It is more accurate than the sensor presented in this work in measuring wind speed but less accurate in measuring the angle. The conversion times used for the measurements are not reported and measuring temperature is not possible with this sensor. This sensor requires the connection of 16 bond wires to the chip.

Table 4.2 summarizes the performance of the three wind sensors. The heater power is equal for all three sensors. The wind measuring accuracy is quite comparable. However, the amount of bond wires required by the sensor and the amount of external electronics is by far the least for the design presented in this work.

	This work	J. Wu[8]	Y. Zhu[15]
Publication year	2015	2011	2015
Technology	0.7μm CMOS	0.7μm CMOS	MEMS(SIG)
Open-/Closed-loop	Closed-loop	Closed-loop	Open-loop
Read-out circuit	On-chip	On-chip	Off-chip
No. of bond wires	8	12	16
Wind speed range	1-25m/s	1-25m/s	0-25m/s
Power consumption	25mW	25mW	25mW
Decimation filter	fixed sinc[1]	tracking sinc[2]	N/A
Speed error	6 % *	4 %	2.5%
Direction error	± 2°*	± 2°	± 6°
Temp. meas. freq.	1Hz	1/8Hz	N/A
Temperature error	$\pm1.3°C$	± 1°C	N/A
Temp. RMS noise	$\pm1°C$	$\pm0.15°C$	N/A

Table 4.2: In this table the performance of several wind sensors is summarized.
* :The measurements at 1m/s were ignored for the comparison.

Conclusions and recommendations

<div style="text-align: right; font-size: 3em;">5</div>

5.1 Conclusions

In this thesis, a smart wind sensor is presented. The thermal structure of the sensor was modified with respect to prior work to allow for simpler back-end processing and faster temperature measurements. The resulting higher oscillation frequency of the system allows for a much simpler static $sinc^1$ filter to be used to filter out the quantization noise instead of the tracking $sinc^2$ filter used in [10]. With the addition of logic on the sensor chip, the amount of external electronics needed by the sensor system is minimized and the minimal number of bond wires required is lowered by 50%, from 12 to 8.

Three different heater modes (section 3.1.2) were implemented and tested in order to test the behavior of the sensor when scaling the reference power, while keeping the total heater power equal. The normal mode was found to function most like the prior work, as was expected. In RTH mode, the system was found to be more sensitive to thermal gradients and thus it increased the SNR, but the wind measuring accuracy was not improved. The 1-H mode was found to be not linear enough to perform well in the wind measurements. System- and circuit-level design of the sensor are discussed and measurement results are provided to prove the functioning of the sensor.

The sensor was measured in a wind tunnel to validate its performance. For wind speeds between 4 and 25m/s, the sensor achieves wind measuring errors below $\pm 6\%$ (speed) and $\pm 2°$ (direction) with 25mW of heater power. The sensor performs at par with the prior design, except for a small performance degradation at low wind speeds.

The wind sensor can be used to measure temperature by observing the oscillation frequency of the thermal balancing loops. With batch calibration and a 1-point trim an error of $\pm 1.3°C$ was achieved for four sensors. The conversion time is 1 second and the RMS noise $\pm 1°C$. The thermal modifications were expected to improve temperature measurement accuracy of the system, but the measurements show that the measurement noise is too large to achieve good accuracy.

5.2 Recommendations for future work

The following points are recommendations to further the development of the integrated smart wind sensor.

In [10] a Newton-Raphson-based algorithm was used to calculate wind speed and direction using only the wind sensor model from section 2.3. With this algorithm, the

calculations that are performed on the sensor output are simplified. Because no documentation on this algorithm was available, it was not successfully reproduced for use in this work. Implementing it again will be valuable for when the sensor is driven by a low-cost microprocessor.

The corner heater placement has been proven to work, but is not necessarily better then the prior heater placement. This might be due to a too large shift of the oscillation frequency. A heater location in between the current and the previous placement may improve the performance, while still having the benefits of the increased oscillation frequency. Physics-based simulation software such as COMSOL Multiphysics may be used to determine the optimal heater location.

The test heater in the North-East corner has been an important tool to measure the performance of the sensor. For future work it will be valuable to connect a test heater in each corner to a bond pad. This will enable control of the 'direction' of the thermal imbalance created by the test heaters, which makes it a better test instrument. Making the test heaters available for driving when the chip is placed in the wind sensor enclosure can provide insight into the spread that is introduced by the packaging of the sensor. The sensor currently requires a fairly intricate calibration procedure because of this spread. Simplification of the calibration and making it less dependent on the use of a wind tunnel is an important step towards the actual implementation of this sensor in a product and may be enabled.

The temperature measurement accuracy seems to be limited by the high RMS noise. Restoring the noise to the $\pm 0.15°C$ that was achieved in [10] may improve the performance. The increase in noise may be caused by the decrease of the over-sampling ratio when compared to the prior work. This can be restored by increasing the speed of the comparator and the implementing the rest of the system in such a way that the sampling frequency can be increased to get this ratio back to around 500.

Bibliography

[1] Y. Zhu, B. Chen, M. Qin, and Q. Huang, "2-D Micro-Machined Thermal Wind Sensors - A Review," *IEEE Internet of Things Journal*, vol. vol. 1, pp. 216–232, 2014.

[2] M. del Valle, J. Castelán, Y. Matsumoto, and R. Mateos, "Low Cost Ultrasonic Anemometer," *4th Int. Conf. on Electrical and Electronics Engineering (ICEEE 2007)*, pp. 213–216, 2007.

[3] S. Kapartis, "Ultrasonic flow velocity sensor and method of measuring the velocity of a fluid flow," *European Patent EP 0 801 311 A1*, 1997.

[4] B. van Oudheusden, *Integrated silicon flow sensors*. Ph.D Thesis, Delft University of Technology, 1989.

[5] H. Verhoeven, *Smart thermal flow sensors*. Ph.D Thesis, Delft University of Technology, 1996.

[6] K. Makinwa and J. Huijsing, "A Smart CMOS Wind Sensor," *Proc. ISSCC Dig.Tech. Papers*, pp. 432–479, 2002.

[7] J. Wu, Y. Chae, C. van Vroonhoven, and K. Makinwa, "A 50mw cmos wind sensor with 4 % speed and 2 direction error," *Proc. ISSCC Dig.Tech. Papers*, pp. 106–107, 2011.

[8] J. Wu, C. van Vroonhoven, Y. Chae, and K. Makinwa, "A 25mW CMOS sensor for wind and temperature measurement," *Proc. IEEE Sensors*, pp. 1261–1264, 2011.

[9] K. Makinwa, *Flow sensing with thermal sigma-delta modulators*. Ph.D Thesis, Delft University of Technology, 2004.

[10] J. Wu, *A Low-Power Thermal Wind Sensor in CMOS Technology*. M.Sc. Thesis, Delft University of Technology, 2013.

[11] K. Makinwa and J. Huijsing, "Constant Power Operation of a Two-Dimensional Flow Sensor," *IEEE Trans. Instrumentation and Measurement*, pp. 840–844, 2002.

[12] S. M. Kashmiri, *Electrothermal Frequency References in Standard CMOS*. Springer, 2013.

[13] AMI Semiconductor Belgium, *I2T100 Design and Layout Manual, Rev. 7.0*. 2007.

[14] B. van Oudheusden and J. Huijsing, "An electronic wind meter based on a silicon flow sensor," *Sensors and Actuators A: Physical*, vol. 22, pp. 420–424, 1990.

[15] Y. Zhu, B. Chen, M. Qin, J. Huang, and Q. Huang, "Development of a self-packaged 2D MEMS thermal wind sensor for low power applications," *J. Micromech. Microeng.*, vol. 25, 2015.

Complete Wind Measurement Results $\quad$ A
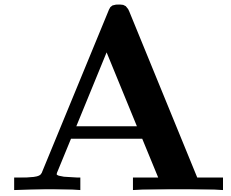
The following pages contain the final wind measurement results for four measured wind sensors. For these measurements, the sensors were operated in normal mode, i.e. without RTH and 1H activated, at 50mW of heating power and at a sampling frequency of 150kHz. The sensors were measured in the wind tunnel at Mierij Meteo BV in De Bilt, The Netherlands. In the wind tunnel the sensors were exposed to winds between 1 and 25m/s from 12 equispaced angles. A picture of the wind tunnel used is shown below.

Sample 3: Abs. speed

Sample 3: Rel. speed

Sample 3: Angle

54

Sample 4: Abs. speed

Sample 4: Rel. speed

Sample 4: Angle

Sample 5: Abs. speed

Sample 5: Rel. speed

Sample 5: Angle

56

Sample 6: Abs. speed

Sample 6: Rel. speed

Sample 6: Angle